International Journal of
Turbomachinery Propulsion and Power

MDPI

Article

Off-Design Aerodynamics of the SPLEEN C1 Cascade

Gustavo Lopes [†], Loris Simonassi [‡], Antonino Federico Maria Torre [§], Marios Patinios [‖] and Sergio Lavagnoli [*]

Turbomachinery and Propulsion Department, von Karman Institute for Fluid Dynamics, Chaussée de Waterloo 72, 1640 Rhode-St-Genèse, Belgium; gustavo.filipe.docarmolopes@edu.unige.it (G.L.)
* Correspondence: sergio.lavagnoli@vki.ac.be; Tel.: +32-(0)2-3599-629
† Current address: DIME, University of Genova, 16126 Genova, Italy.
‡ Current address: Avio Aero, 10040 Turin, Italy.
§ Current address: MTU Aero Engines, 80995 Munich, Germany.
‖ Current address: GE Aerospace, 85748 Garching, Germany.

Abstract

High-speed, low-pressure turbines in geared turbofans operate at transonic exit Mach numbers and low Reynolds numbers. Engine-relevant data remain scarce. The *SPLEEN C1* linear cascade was investigated at $M_{out} = 0.70$–0.95 and $Re_{out} = 65{,}000$–$120{,}000$ under steady inlet flow. Experiments were combined with 2D RANS and MISES, including transition modeling and inlet-turbulence decay calibrated to measurements. Results are consistent with conventional LPT behavior: loss decreased with increasing Mach and Reynolds numbers, except when shocks interacted with the blade boundary layer ($M \approx 0.95$). Profile loss dropped by 23% from $M = 0.70$ to 0.95 at $Re = 70{,}000$, as well as by 19% at $M = 0.80$ when open separation is suppressed. Secondary loss decreased by up to 25% at $Re = 70{,}000$ and showed weak sensitivity to the Reynolds number. A coupled loss model predicted profile loss with a root-mean square error of 4.7%. Secondary-loss modeling reproduced global trends: separating endwall dissipation from mixing kept errors within $\pm 10\%$ for most cases, but accuracy degraded near the shock–boundary layer interaction case and at the highest Reynolds number. Mixing dominated endwall loss ($\sim$75%), with the passage vortex contributing $\sim$50% ($\pm 10\%$) of the mixing component.

Keywords: high-speed low-pressure turbine; linear cascade; transonic; laminar separation bubble; secondary flows; profile loss; geared turbofan; open-access dataset

1. Introduction

Ultra-high-bypass-ratio geared turbofans (GTFs) reduce CO_2 and noise. For bypass ratios > 10, they enable lower specific fuel consumption, fewer low-pressure turbine stages, and reduced engine mass [1] (the low-pressure turbine (LPT) can account for one-third of the engine mass [2]).

Torre et al. [3] investigated a high-speed LPT in a transonic rotating rig and documented the key differences from conventional LPT operation. In geared architectures, the higher shaft speed drives the LPT blading sections to transonic exit Mach numbers ($M_{out} > 0.80$) and low Reynolds numbers at cruise [4]. This combined transonic/low-Reynolds number regime is a principal challenge for GTF LPT design [5,6].

Hodson et al. [7] showed that loss in axial turbines arises from endwall secondary flows, profile loss, and tip leakage, which have comparable magnitudes. However, low-pressure turbines feature higher aspect ratio blading, leading to profile loss typically dominating over endwall and tip leakage losses [2].

Check for updates

Academic Editor: Marcello Manna

Received: 9 September 2025
Revised: 15 December 2025
Accepted: 30 January 2026
Published: 2 March 2026

Copyright: © 2026 by the authors. Published by MDPI on behalf of the EUROTURBO. Licensee MDPI, Basel, Switzerland. This article is an open access article distributed under the terms and conditions of the Creative Commons Attribution (CC BY-NC-ND) license.

Vera et al. [8] showed that profile loss is nearly independent of Mach up to $M \approx 0.76$ and rises beyond at $Re = 190{,}000$. Vázquez et al. [9] observed increasing loss with Mach and decreasing loss with the Reynolds number in an annular cascade. Both works attributed the Mach effect to higher dynamic pressure and altered suction side loading [8,9].

Perdichizzi [10] reported that higher outlet Mach confines secondary structures toward the endwall, reducing under/overturning and net loss. The Mach and Reynolds effects were not decoupled for LPT conditions. Vázquez et al. [9] found endwall loss decrease with off-design Mach at a fixed Reynolds number. Vázquez and Torre [11] confirmed the Mach effect at fixed incidence and linked it to off-design loading changes.

Hodson and Dominy [12] reported increasing secondary loss with the Reynolds number near $M \approx 0.70$. Duden and Fottner [13] found secondary loss decreasing as both Mach and Reynolds increased for other LPT blades.

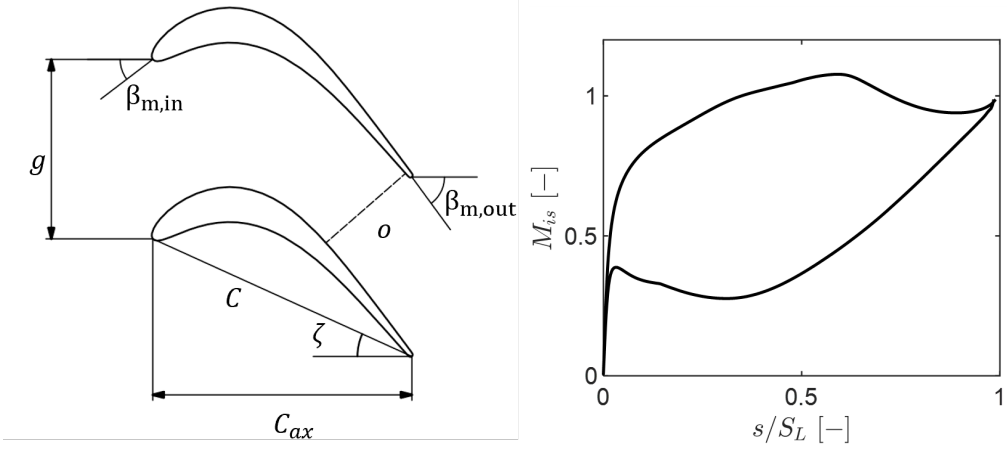
Despite these findings in the literature, few studies have targeted a combined high Mach number, very-low-Reynolds number regime (~70,000) that can exist in high-speed LPT blading. To our knowledge, no open database provides on- and off-design measurements for a high-speed LPT linear cascade.

This study extends the open *SPLEEN C1* test case. The operating points spanned $M_{out} = 0.70$–0.95 and $Re_{out} = 65{,}000$–$120{,}000$ under a steady inlet flow. Experiments were combined with 2D Reynolds-averaged Navier–Stokes (RANS) computations and MISES with transition modeling. Inlet turbulence decay was calibrated to hot-wire measurements. Separation and reattachment were identified using an acceleration parameter method that was anchored to the data. Profile and secondary loss were decomposed, and loss models were assessed under high-speed LPT conditions. This study builds upon and expands ref. [14]. The data presented in this study are openly available in Zenodo at https://doi.org/10.5281/zenodo.7264761 [15] (accessed on 12 December 2025).

2. Experimental Methods

2.1. The SPLEEN C1 Test Case

The *SPLEEN C1* test case, introduced in [16], considers the rotor-hub geometry of a geared low-pressure turbine. The profile was designed for $M_{out} = 0.90$ and $Re_{out} = 70{,}000$. The Reynolds number is based on outlet aerothermodynamic conditions and the true chord C. The blade that was used in the experiments is shown in Figure 1a. The nominal blade loading from a turbulent RANS solution is shown in Figure 1b. Key geometric parameters are listed in Table 1.



(**a**) (**b**)

Figure 1. *SPLEEN C1* geometry (**a**) and the blade loading at the design point (**b**).

Table 1. *SPLEEN C1* cascade key geometrical features.

Parameter	Value	Unit
True chord, C	52.285	[mm]
Axial chord, C_{ax}	47.614	[mm]
Pitch-to-chord ratio, g/C	0.630	[−]
Cascade span, H	165	[mm]
Aspect ratio, H/C_{ax}	3.47	[−]
TE thickness, δ_{TE}	0.86	[mm]
TE radius/C	0.0082	[−]
TE wedge angle	4.96	[°]
Throat, o	19.400	[mm]
Inlet metal angle, $\alpha_{met,in}$	37.30	[°]
Outlet metal angle, $\alpha_{met,out}$	53.80	[°]
Stagger angle, ζ	24.40	[°]
Diffusion factor, DF	18	[%]
Circulation coefficient, C_0	0.61	[−]
Zweifel coefficient, Z_w	0.73	[−]

The cascade, built of 23 blades, had an aspect ratio (based on span and axial chord) of 3.5:1, which is representative of modern low-pressure turbine applications [2]. A passive turbulence grid sets a freestream turbulence intensity of $TI \approx 2.40\%$. A spoked-wheel wake generator with 96 cylindrical bars of a 1.00 mm diameter can impose unsteady wakes. The bar diameter matched the trailing edge thickness and produces an airfoil-like wake [17]. The bars extended to ∼73% of the span when aligned with the central blade leading edge. At midspan, the reduced frequency was $f^+ \approx 0.95$ and the flow coefficient was $\Phi \approx 0.80$ [18–20]. A slot between the wake generator and the cascade allowed for purge injection with a purge mass-flow ratio of 0–1% [21]. In this study, the wake generator and the purge system were off.

2.2. The VKI S-1/C High-Speed Linear Cascade

Measurements were conducted in the high-speed, low-Reynolds number facility S-1/C at the von Karman Institute. The tunnel is a continuous closed loop driven by a 615 kW, 13-stage axial compressor. A heat exchanger holds the flow near ambient temperature. Mass flow is set by compressor speed and a pressure-control valve. A vacuum pump enables static pressures as low as 5000 Pa.

Figure 2 shows the wind-tunnel layout. The cascade test section is located in the first elbow after the diffuser. Wire meshes and honeycombs condition the flow. The facility covers high-subsonic to transonic exit conditions. A movable turbulence grid sets the freestream turbulence level. Unsteady wakes can be imposed with a spoked-wheel wake generator. A secondary air system supplies purge flow. Descriptions of the facility and its components can be found in [19–21] and in the open database at https://doi.org/10.5281/zenodo.7264761 [15] (accessed on 12 December 2025).

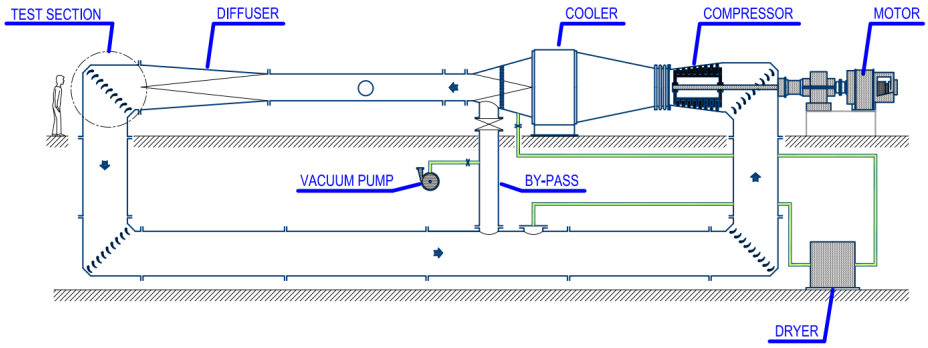
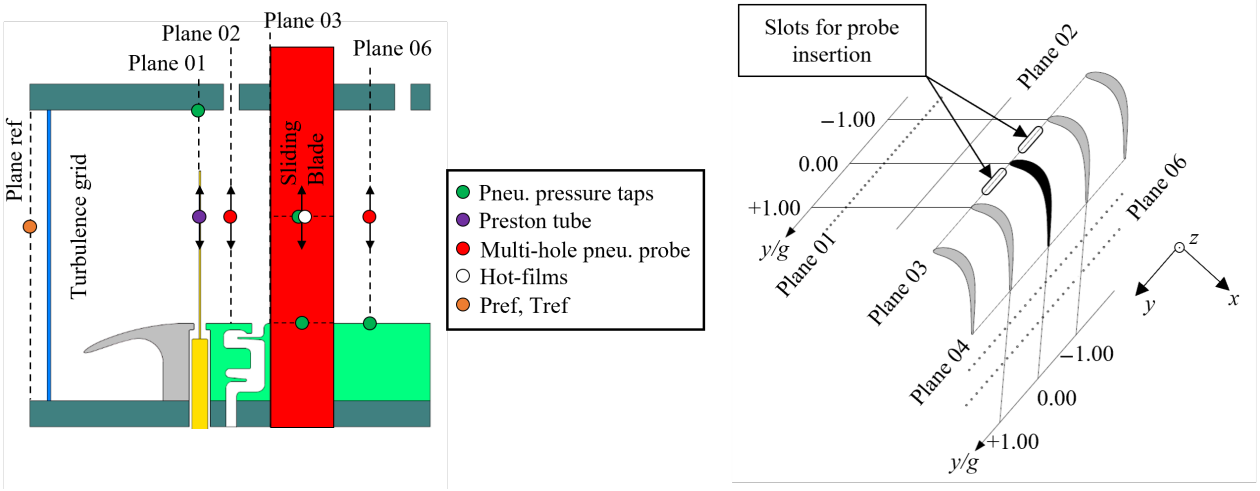


Figure 2. The VKI S-1/C wind tunnel.

2.3. Instrumentation

Figure 3a shows a meridional view of the test section and the measurement planes in the cascade reference frame. Figure 3b shows a blade-to-blade view. The pitchwise coordinate y increases toward passages below the central blade. The origin at each plane is the intersection between the measurement plane and the plane formed with the leading edge at the inlet metal angle. Downstream, the same construction uses the trailing edge and the outlet metal angle.



(**a**) (**b**)

Figure 3. The test section layout and instrumentation (**a**), as well as the blade-to-blade view (**b**).

Fixed instrumentation monitored the rig operating condition. Isentropic inlet and outlet Mach numbers and Reynolds numbers were computed from the inlet total pressure downstream of the grid, the inlet total temperature, and the inlet and outlet static pressures. The cascade inlet total pressure was not measured. A correlation was used to estimate the pressure drop across the turbulence grid and the wake generator as a function of the flow condition. The correlation mapped the measured reference total pressure upstream of the grid to the cascade inlet total pressure [16].

The reference total pressure and temperature were measured with a WIKA P-30 absolute pressure sensor and a bare K-type thermocouple. The static pressure at Plane 06 was measured 0.50 C_{ax} downstream of the trailing edge. The inlet flow at Plane 02 was surveyed with a Cobra-shaped five-hole probe (C5HP). The outlet flow at Plane 06 was surveyed with an L-shaped five-hole probe (L5HP). Probe ports were connected to a Scanivalve MPS4264 (1 psi). Aerodynamic calibration coefficients were applied to recover the local total pressure and flow angles [18]. When the L5HP was not installed, the static

pressure for the kinetic energy loss calculations was interpolated from pressure taps at Plane 06.

Blade loading was measured with surface pressure taps. The suction side had 24 taps, and the pressure side had 17 taps. The endwall pressure distribution within the passage was also mapped using pneumatic pressure taps. The taps were integrated into two inserts on the endwalls: Insert 1 above the central blade and Insert 2 below it. Insert 1 contained thirty pneumatic taps, while Insert 2 held thirty-six pneumatic taps.

Two Scanivalve MPS4264 units with ranges of 1 psi and 2.5 psi recorded the pressures from the probes, Plane 06 taps, blade taps, and passage taps. Surface-mounted hot-film sensors measured the quasi-wall shear stress. The suction and pressure sides had 31 and 21 sensors at 2 mm spacing. The array was custom-built by Tao Systems. It wrapped around the leading edge and sat in a flush recess on both sides. These measurements were also used to assess the secondary flow and wake effects [19,20]. A full description of the sensor geometry and operation is given in [18].

Signals were conditioned with a Dantec Streamline Pro using six Wheatstone bridges. The 52 channels were acquired in groups. Signals were low-pass filtered at 8 kHz. Acquisition used an NI6253-USB board at 1200 kHz for 3 s.

Uncertainty estimates for the measured and derived quantities are reported in Table 2. The random and systematic components used a 95% confidence interval. A detailed uncertainty budget and propagation are provided in [18].

Table 2. Breakdown of the experimental uncertainty with a 95% confidence interval.

Instrument	Qt.	Unit	U_{rand}	U_{sys}
Fixed	T_{01}	K	0.01	0.52
	$P_{01,fs}$	Pa	7.01	29.82
Blade pneu./Endwall pneu.	M_{is}	–	0.001	0.005
Preston tube	V_{BL}/V_{fs}	–	0.001	0.008
C5HP	inc	°	0.31	0.98
	M	–	0.002	0.010
L5HP	$\beta-\beta_{MS}$	°	0.15	0.33
	ξ	–	0.002	0.010
HW	TI	% of u	–	0.20%
	ILS	mm	–	3.92

2.4. Flow Conditions

The on- and off-design operating points were investigated. Instrument deployment varied across the test matrix. Table 3 summarizes the instrumentation that was used at each $(M_{\text{out}}, Re_{\text{out}})$: aerodynamic probes (APs), blade pneumatic taps (BPs), endwall pneumatic taps (EPs), and blade surface-mounted hot films (HFs).

Table 3. The instrumentation by operating condition. AP: aerodynamic probe. BP: blade pneumatic tap. EP: endwall pneumatic tap. HF: hot film.

		M [−]			
		0.70	**0.80**	**0.90**	**0.95**
Re [−]	65,000	BP/EP	BP	BP/EP	BP
	70,000	AP/BP/HF	AP/BP	AP/BP/HF/EP	AP/BP/HF/EP
	100,000	BP	BP	BP/EP	BP/EP
	120,000	BP/HF	AP/BP	AP/BP/HF/EP	BP

3. Numerical Methods

MISES and RANS were used to complement the experiments and to obtain blade loading and boundary layer parameters for loss modeling. MISES is a coupled viscous–inviscid solver that combines steady Euler equations with integral boundary layer equations [22]. It includes a modified Abu–Ghannam and Shaw transition model, as described by Drela [23,24].

The RANS computations used *Cadence Fine*^{TM}*/Turbo 18.2*. The turbulence closure used the k–ω SST model. Transition was modeled with the γ–$\tilde{R}e_{\theta t}$ model of Langtry and Menter [25]. The inlet boundary conditions were the total pressure, total temperature, flow direction, and turbulence quantities. The outlet boundary condition was static pressure. The total-to-static pressure ratio was adjusted to match the experimental M_{out} and Re_{out} at $T_0 = 300$ K.

The turbulent kinetic energy k and dissipation rate ϵ at the inlet were prescribed from the measured turbulence intensity TI and the integral length scale ILS:

$$k = \frac{3}{2}(U_{in}\, TI)^2, \tag{1}$$

$$\epsilon = C_{\mu}^{3/4}\, \frac{k^{3/2}}{ILS}, \tag{2}$$

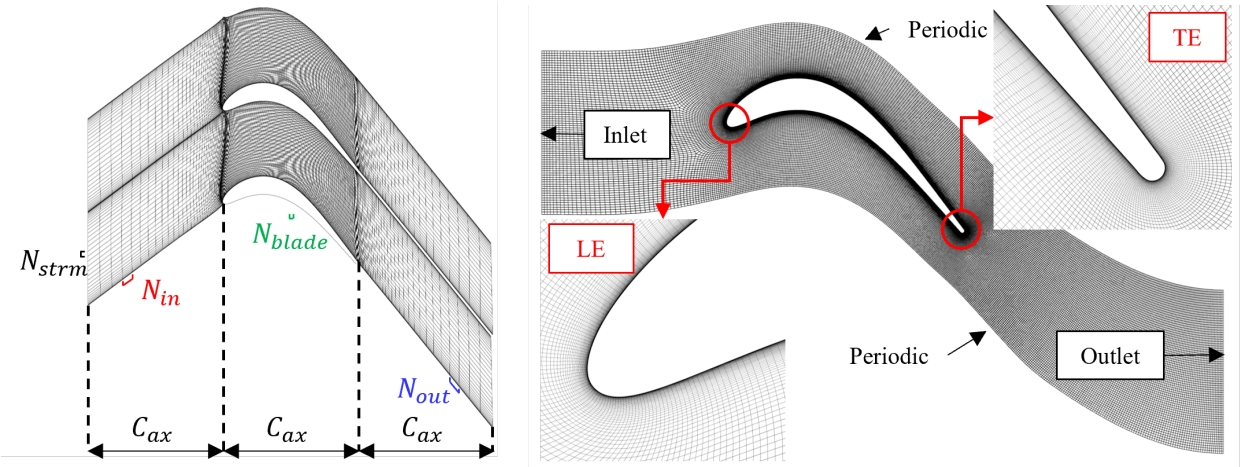
with $C_{\mu} = 0.09$. Sensitivity to the inlet flow angle was assessed in MISES and RANS. Blade loading was insensitive within the measured incidence range. An incidence of -0.60° was found to provide the best agreement between the experiments and numerical results for all cases [18].

3.1. Mesh

Mesh sensitivity studies were performed for MISES and RANS. For MISES, additional refinement had a negligible effect on the blade loading. The final MISES mesh is shown in Figure 4a and is summarized in Table 4.

Table 4. Mesh parameters for the MISES computations.

N_{strm}	N_{in}	N_{out}	N_{blade}	Total Elements
40	40	40	200	10,803



(**a**) (**b**)

Figure 4. Final meshes for MISES (**a**) and RANS (**b**).

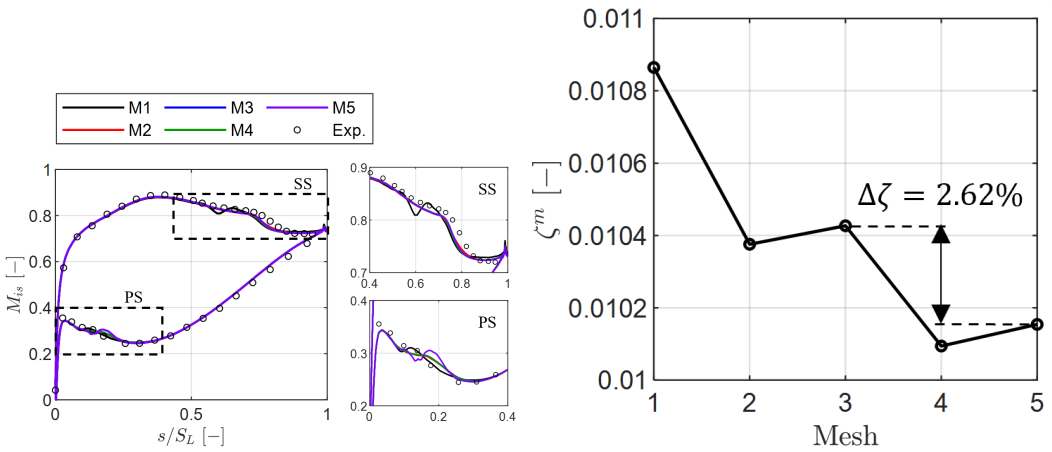
The structured RANS meshes were generated with *Autogrid5*. An O-block topology wraps the blade. The number of nodes on the suction and pressure sides sets the near-wall resolution. The final RANS mesh and topology are shown in Figure 4b.

Five RANS meshes, with approximately 50,000 to 180,000 cells, were tested. The mesh was designed following the guidelines of Langtry [26] for the γ–$\tilde{Re}_{\theta t}$ transition model. Near the blade, $y^+ < 1$ was enforced with a first cell height of approximately 2 µm. The wall-normal expansion ratio was 1.05 in the boundary layer region, with approximately 77 cells placed within the boundary layer thickness ($\delta \approx 2$ mm at the aft suction side). These parameters ensure adequate resolution of the laminar boundary layer and transition region. The mesh properties are listed in Table 5.

Table 5. The RANS meshes for the sensitivity study.

Name	N_{SS}	N_{PS}	N_{tot}	Max. ER	Max. y^+
M1	137	121	∼50,000	1.05	1.02
M2	177	157	∼80,000	1.05	0.64
M3	209	189	∼115,000	1.05	0.38
M4	241	213	∼150,000	1.05	0.26
M5	261	229	∼180,000	1.05	0.13

Figure 5a shows the surface isentropic Mach number for $M = 0.70$ and $Re = 120{,}000$. The overall loading was weakly sensitive to the mesh density. A close-up of the suction side near the trailing edge showed that the mesh density affected the laminar separation bubble topology. The coarsest mesh exhibited oscillations. Differences among the other meshes were small. On the pressure side, oscillations appeared for the coarsest and the finest meshes because the separation bubble was unsteady.



(**a**) (**b**)

Figure 5. The RANS mesh sensitivity for $M = 0.70$ and $Re = 120{,}000$. (**a**) The surface isentropic Mach number along the normalized surface length. (**b**) The mass-averaged total-pressure loss coefficient.

Figure 5b reports the mass-averaged total-pressure loss coefficient. The relative errors for M3 and M4 against the most refined mesh were 2.62% and 0.69%. For M3, the absolute difference was $\Delta\zeta = 3 \times 10^{-4}$. Mesh M3 was, therefore, considered sufficiently converged for this case.

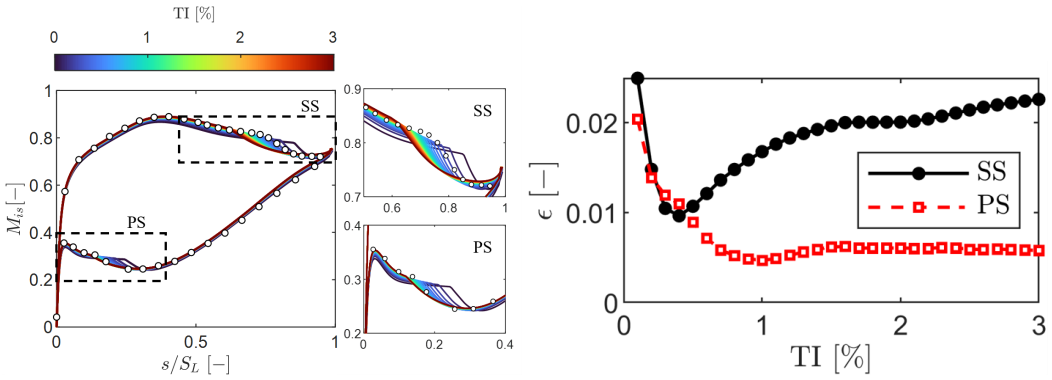
3.2. Turbulence Model Calibration

MISES was used to calibrate the blade loading to reproduce the suction side laminar separation bubble. For the AGS transition model, only the inlet turbulence intensity was required. The intensity was swept from 0.10% to 3.00% in 0.10% steps. The case

where $M = 0.70$ and $Re = 120{,}000$ was selected because it exhibited a closed laminar separation bubble.

Figure 6a shows the surface isentropic Mach number. The aft suction side was sensitive to the prescribed turbulence intensity. At the measured free-stream level (≈2.40%), a bubble appeared but was smaller than in the experiments. Reducing the intensity enlarged the bubble and improved the suction side agreement. The pressure side was also affected, and the agreement worsened as the intensity was reduced. The misfit was quantified with

$$\epsilon = \sqrt{\frac{1}{N}\sum_{i=1}^{N}\left(M_{\mathrm{exp},i} - M_{\mathrm{MISES},i}\right)^2}. \tag{3}$$



(**a**) (**b**)

Figure 6. Sensitivity to the turbulence intensity. (**a**) The surface isentropic Mach number along the normalized surface length. (**b**) The relative error ϵ between MISES and the experiments.

Errors on the suction side were computed between the velocity peak and the last sensor before the trailing edge. Errors on the pressure side were computed between the second tap and the point of the minimum Mach number. Figure 6b reports ϵ versus the intensity. An intensity of 0.40% maintained the suction side error below 0.01 and was, therefore, adopted for MISES across all cases, where the suction side fidelity was prioritized given its dominant role in profile loss [27].

For the RANS inlet, κ and ϵ were adjusted to match the turbulence intensity level, and the decay was measured with a cross-wire probe [28], following the procedure in [29]. Figure 7 compares the measured decay and a fitted power law with the Roach correlation [30]. The central blade leading edge is 0.40 m downstream of the grid, and the $y/g = 0$ location at Plane 02 is indicated. Using the measured integral length scale (∼12 mm) produced a decay that was too slow relative to the fitted curve. Fine tuning the inlet turbulence parameters, as in [31], yielded a good match with TI ≈ 2.60% and an effective integral length scale (ILS ≈ 0.93 mm).

In RANS, the apparent turbulence level increases toward the leading edge because the decay distance was measured normal to the grid. In the experiment, the traverse at Plane 02 remained parallel to the leading edge plane, so the effective distance varied with a pitchwise position. The same tuning procedure was applied to all operating points. The resulting inlet κ, ϵ, TI, and ILS used in the computations are listed in Table 6.

It is useful to compare the computational cost. MISES was substantially cheaper, with a typical operating point converging in $\approx 1.1 \times 10^{-3}$ CPU-h. The 2D RANS calculations with transition were initialized from a converged fully turbulent solution to improve numerical stability; the mean costs were ∼0.30 CPU-h for the turbulent initialization and ∼1.58 CPU-h for the transitional run. The resulting cost ratio between RANS (turbulent + transition) and MISES was ≈3.2 orders of magnitude.

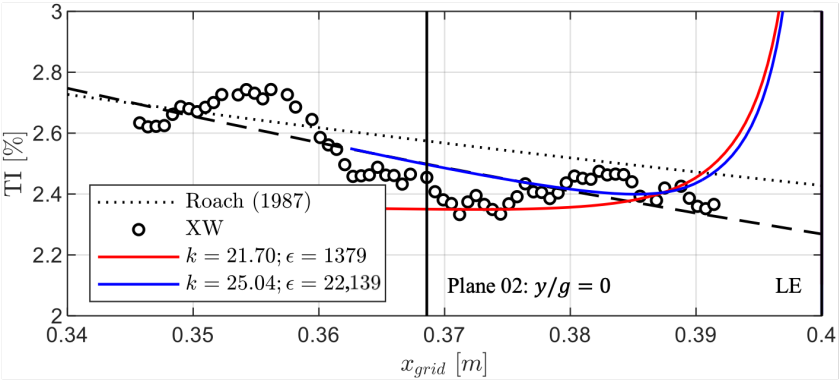


Figure 7. The RANS inlet turbulence decay tuned to cross-wire data and compared with the Roach correlation [30].

Table 6. The RANS inlet turbulence parameters matching the experimental decay.

M_{out} [−]	Re_{out} [−]	k [m²/s²]	ϵ [m²/s³]	TI [%]	ILS [mm]
0.70	65,000	20.396	16275	2.60	0.93
0.80	65,000	23.585	20237	2.63	0.93
0.90	65,000	24.991	22074	2.63	0.93
0.70	70,000	20.733	16680	2.62	0.93
0.80	70,000	23.656	20329	2.63	0.93
0.90	70,000	25.067	22175	2.62	0.93
0.95	70,000	25.086	22200	2.60	0.93
0.70	100,000	21.269	17331	2.63	0.93
0.80	100,000	23.719	20410	2.63	0.93
0.90	100,000	25.271	22446	2.63	0.93
0.95	100,000	25.486	22733	2.63	0.93
0.70	120,000	21.585	17718	2.65	0.93
0.80	120,000	24.066	20859	2.64	0.93
0.90	120,000	25.370	22578	2.62	0.93
0.95	120,000	25.600	22885	2.61	0.93

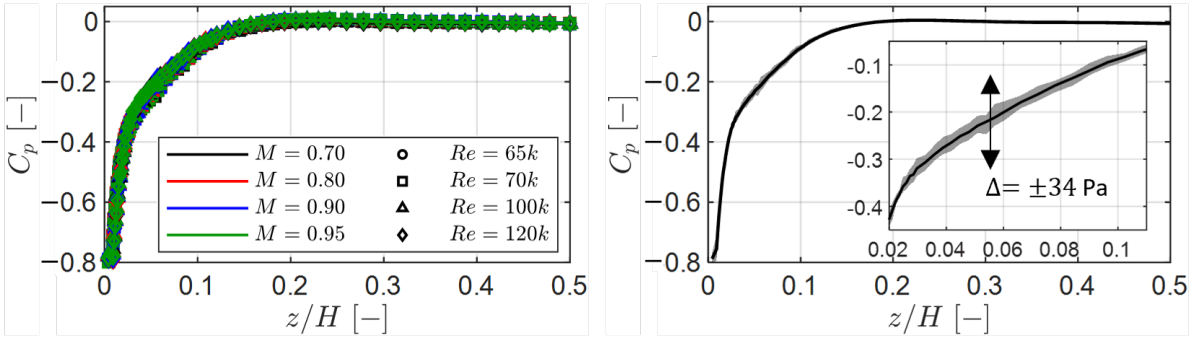
4. Results

4.1. Inlet Boundary Layer Characterization

The inlet boundary layer at Plane 01 was surveyed with a Preston tube under steady flow. The pressure coefficient was

$$C_p = \frac{P_{\mathrm{BL}} - P_{01,\mathrm{fs}}}{P_{01,\mathrm{fs}} - P_1}, \tag{4}$$

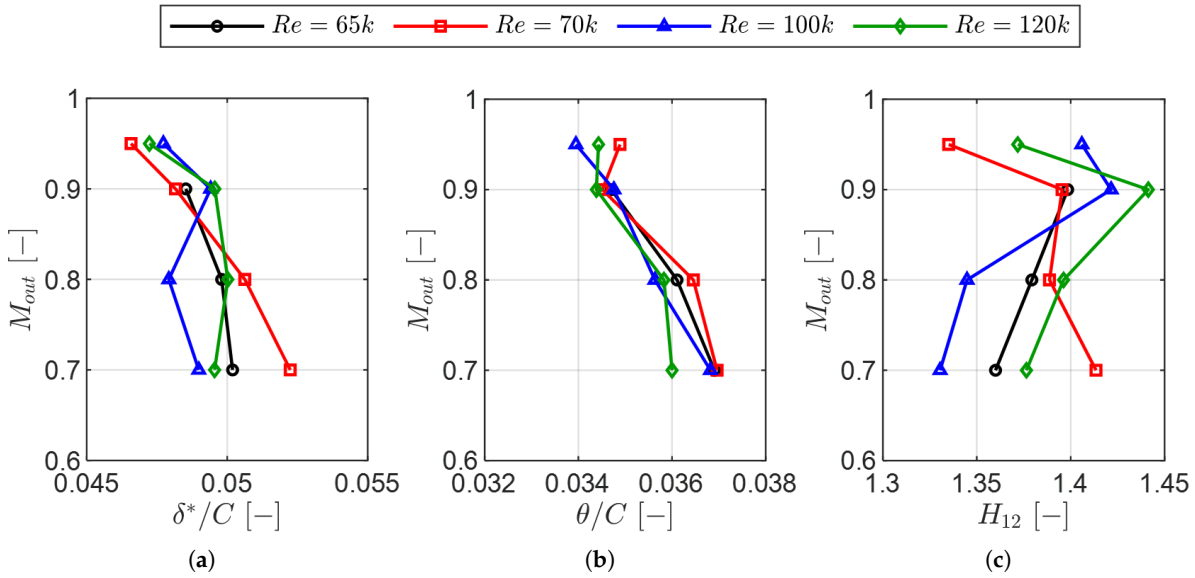
where P_{BL} is the Preston pressure, $P_{01,\mathrm{fs}}$ is the freestream total pressure, and P_1 is the endwall static pressure at Plane 01. Figure 8a shows the spanwise distribution of C_p for the on- and off-design conditions. The curves for all flow conditions nearly overlapped, indicating a strong insensitivity to the range of operating points investigated. Figure 8b reports the maximum local variation across all cases along the span as a shaded band. The inlet total-pressure variation remained within ±0.4% of the inlet freestream total pressure.



(**a**) (**b**)

Figure 8. The inlet boundary layer at Plane 01. (**a**) The spanwise C_p for all conditions. (**b**) The spanwise mean with range (shaded).

Figure 9 summarizes the integral parameters. The displacement thickness decreased with the Mach number and showed no clear Reynolds number trend, with $\Delta\delta^* \approx \pm 0.15$ mm (Figure 9a). The momentum thickness behaved similarly, with $\Delta\theta \approx \pm 0.08$ mm (Figure 9b). The shape factor stayed near $H_{12} \approx 1.38$ for all cases, indicating a turbulent boundary layer [32] (Figure 9c). Within the measurement uncertainty, the inlet boundary layer was insensitive to the operating point.



(**a**) (**b**) (**c**)

Figure 9. The inlet boundary layer integral parameters versus the operating point. (**a**) Displacement thickness. (**b**) Momentum thickness. (**c**) Shape factor.

4.2. Inlet Flow at Plane 02

The midspan pitchwise traversed with the C5HP provided incidence, cascade pitch angle, and velocity profiles.

Figure 10a shows the pitchwise distribution of the incidence. The incidence monotonically decreased across the pitch. The variation was ±1.0° within a given operating point and ±0.24° across all operating points at a fixed pitch location. The mean incidence was ≈−1.0°.

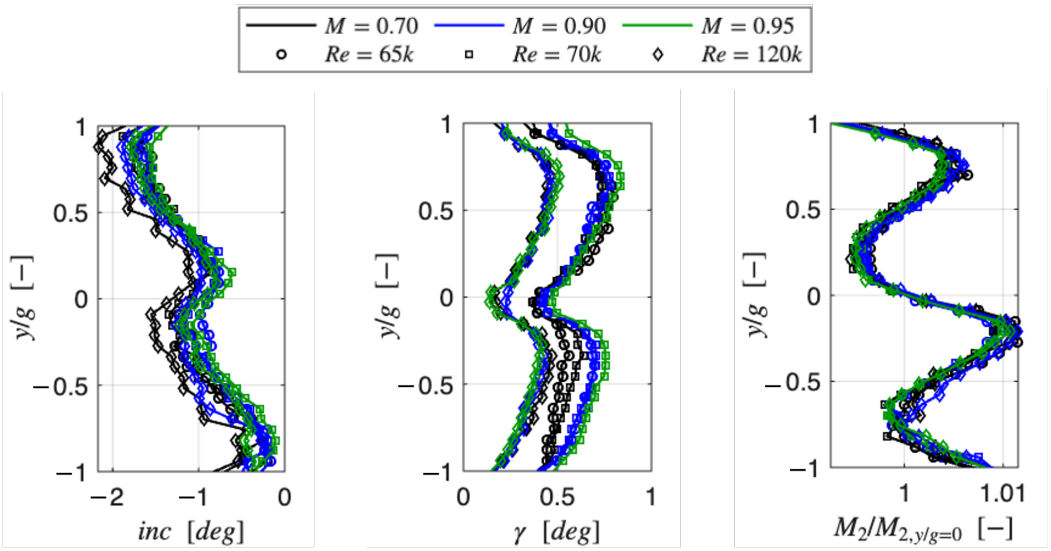


Figure 10. The midspan inlet flow at Plane 02: the (**a**) incidence, (**b**) cascade pitch angle, and (**c**) normalized Mach number.

The cascade pitch angle (Figure 10b) depends on the Reynolds number. At a fixed pitchwise location, a higher Reynolds number yields a lower pitch angle. For a given Reynolds number, the pitch angle is insensitive to the Mach number and shows negligible pitch-to-pitch variation. The near-zero mean angle indicates two-dimensional midspan flow.

The normalized inlet Mach profiles (Figure 10c) collapsed across operating points. The midspan velocity distribution was, therefore, independent of $(M_{\text{out}}, Re_{\text{out}})$.

4.3. Blade Aerodynamics

Figure 11 compares the midspan blade loadings from the experiments, RANS, and MISES at the on- and off-design conditions. Overall agreement was good on both the suction and pressure sides. A systematic underprediction of the suction side Mach level appeared and grew with increasing Mach number. The incidence effects were negligible because the measured incidence was essentially the same for all cases. As the off-design Mach number increased, the velocity peak shifted toward the trailing edge, consistent with the prior observations in cascades by Vázquez et al. [9], Vázquez and Torre [11], and Vera et al. [8].

A suction side close-up is provided in Figure 12. Despite the overall consistency, both solvers struggled to match the aft suction side loading for $M \gtrsim 0.90$, independent of Re, as has also been reported in previous numerical studies on the same test case [33].

At the lowest Mach number, a closed laminar separation bubble formed on the suction side for $Re \geq 100{,}000$ (Figure 12c,d). Reattachment occurred well upstream of the trailing edge. Both CFD and MISES reproduced the bubble topology and length when the calibrated transition settings were used. Similar behavior was found at $M = 0.80$.

For $Re = 65{,}000$ (Figure 12a) and $Re = 70{,}000$ (Figure 12b), the bubble shifted downstream and reattached near the trailing edge. CFD underpredicted the suction side Mach level at the lowest Mach number in these two cases, whereas MISES matched the loading after adjusting the turbulence intensity. The pressure side separationwas also captured by both solvers (see [18] for details).

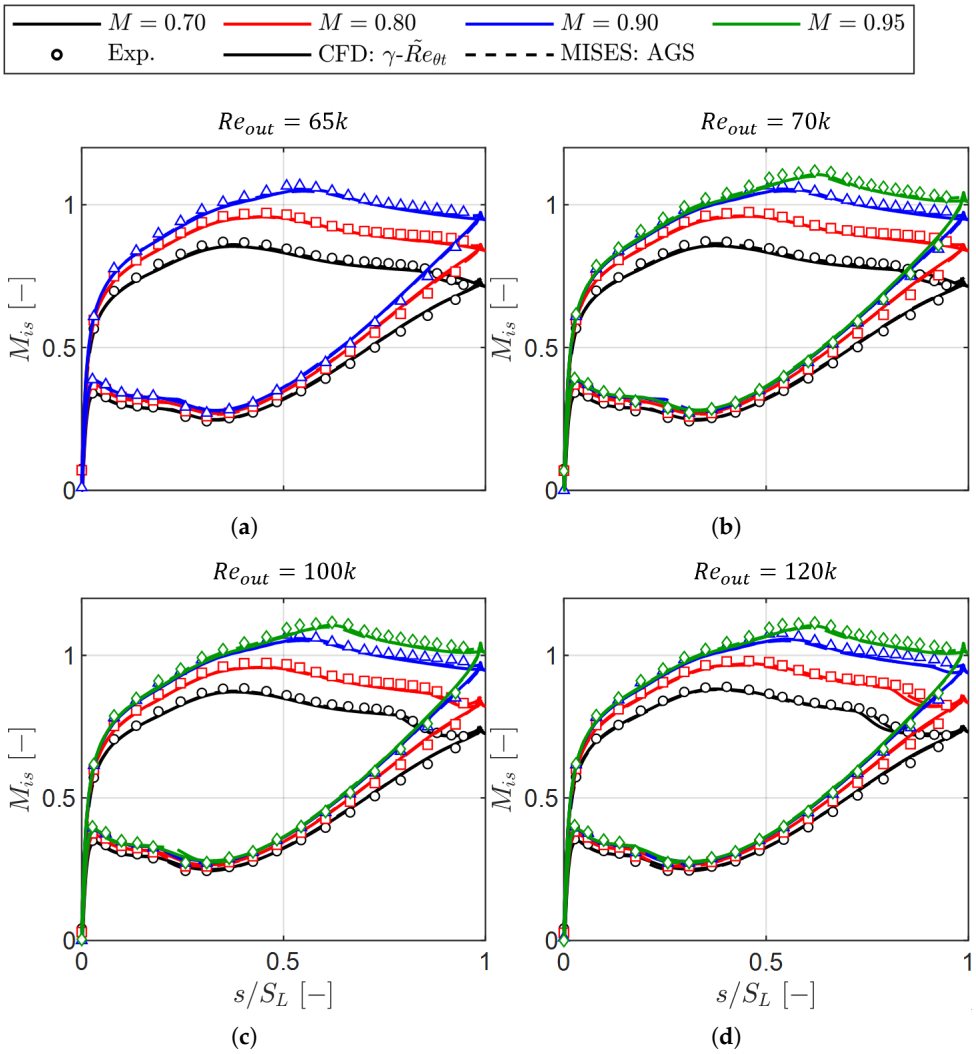


Figure 11. Blade loading: experimental (markers), CFD γ–$\tilde{R}e_{\theta t}$ (solid), and MISES AGS (dashed). $Re = 65{,}000$ (**a**), $Re = 70{,}000$ (**b**), $Re = 100{,}000$ (**c**), and $Re = 120{,}000$ (**d**).

Quasi-wall shear stress from surface hot films was used to locate the separation and reattachment on the suction side. Significant scatter was observed, primarily due to operating at low density and post-test uncertainty in the hot-film bridge offset voltage. The quasi-wall shear stress formulation required a reference voltage at zero velocity, ideally at test conditions. In the S-1/C closed-loop facility, offsets were acquired after rig shutdown, at lower temperatures and without the blade pressure distribution present during testing. Additionally, with 52 sensors and only 6 anemometer channels, the measurement chain could not be optimized for each sensor location. A representative case with a well-defined bubble is shown in Figure 13.

The bubble extent was then inferred from the blade-mounted pneumatic taps using a method based on the acceleration parameter [34,35]:

$$K_s = \frac{\nu}{V_{is}^2} \frac{\partial V_{is}}{\partial s}. \tag{5}$$

Figure 14a shows the suction side M_{is} (black, left axis), the acceleration parameter K_s (red, right axis), and its derivative $\mathrm{d}K_s/\mathrm{d}s$ (blue, right axis) for $M = 0.70$ and $Re = 120{,}000$. All curves were derived from the measurements. K_s and $\mathrm{d}K_s/\mathrm{d}s$ come from a cubic spline fit to the loading.

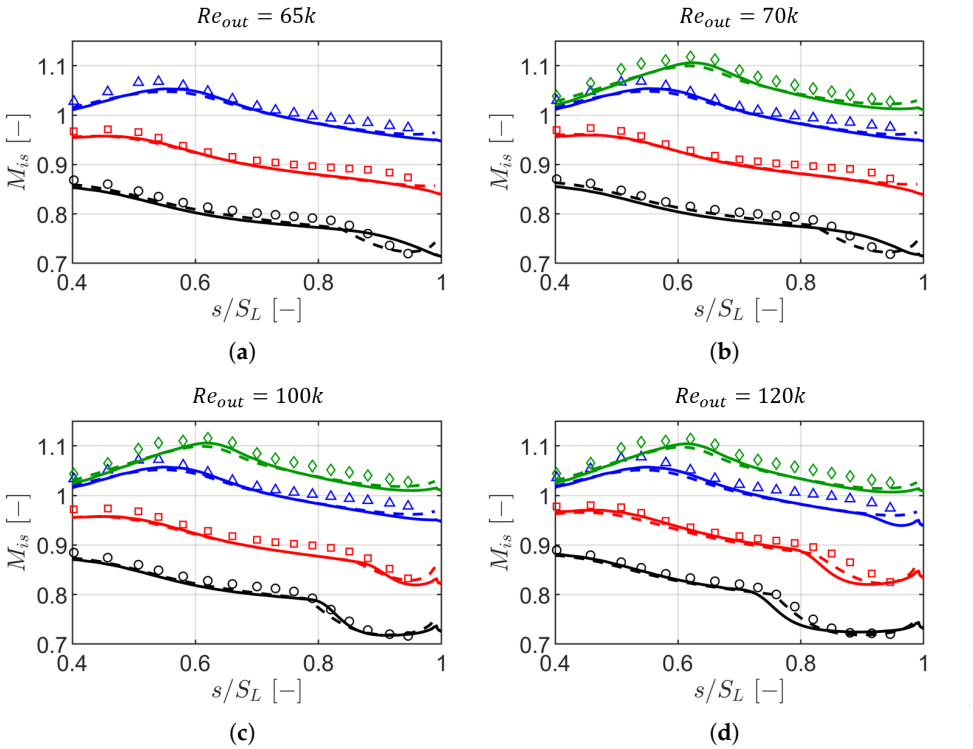


Figure 12. Suction side close-up: experimental (markers), CFD γ–$\tilde{R}e_{\theta t}$ (solid), and MISES AGS (dashed). $Re = 65{,}000$ (**a**), $Re = 70{,}000$ (**b**), $Re = 100{,}000$ (**c**), and $Re = 120{,}000$ (**d**).

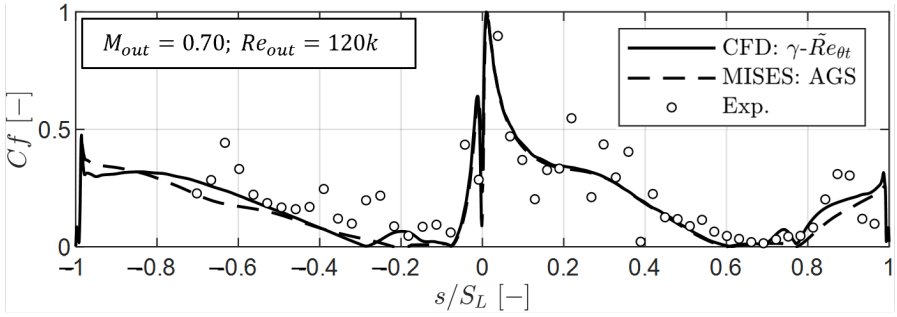


Figure 13. Blade quasi-wall shear stress: experimental (markers), CFD γ–$\tilde{R}e_{\theta t}$ (solid), and MISES AGS (dashed). Negative values were relative to the pressure side.

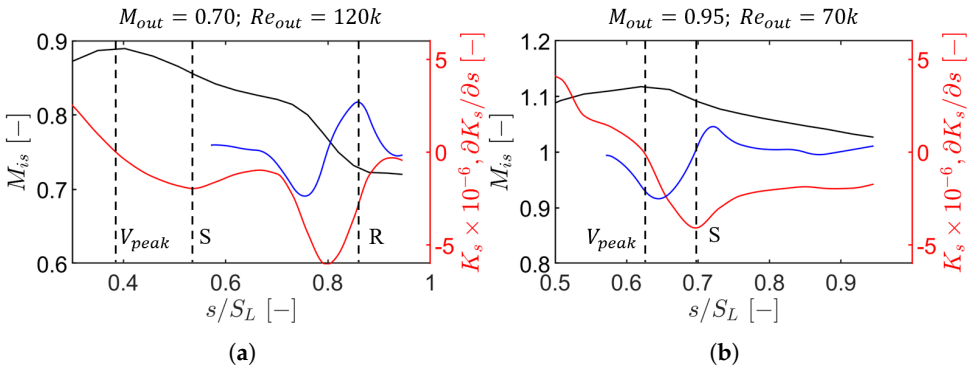


Figure 14. Suction side M_{is} (black, left axis), acceleration parameter K_s (red, right axis), and scaled $\mathrm{d}K_s/\mathrm{d}s$ (blue, right axis). $M = 0.70$, $Re = 120{,}000$ (**a**) and $M = 0.95$, $Re = 70{,}000$ (**b**).

Separation S was taken near the first local minimum of K_s after the velocity peak, where acceleration stopped. Reattachment R was taken at the subsequent inflection in

dK_s/ds, which reflected the bubble imprint on the loading. For $M \leq 0.90$, these signatures were clear. At $M = 0.95$, the aft loading flattened and the shock–boundary layer interaction masked the K_s markers (Figure 14b).

The method was calibrated against CFD and MISES using locations based on the skin friction coefficient. Figure 15 compares the separation positions from C_f and from K_s. A linear fit quantified the lag, excluding $M = 0.95$, where the shocks altered the signature:

$$\text{Sep.}_{C_f} = 1.1031\,\text{Sep.}_{K_s} + 0.0197\,. \tag{6}$$

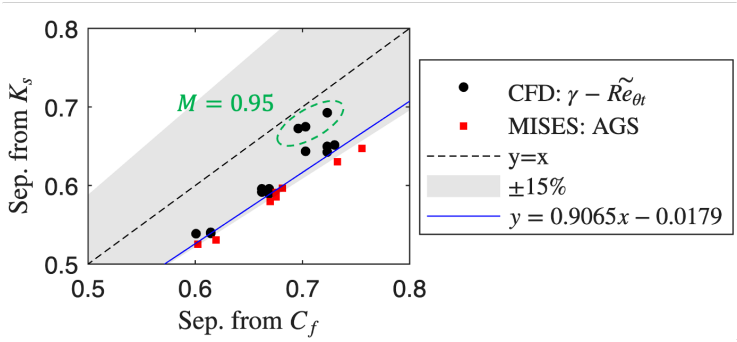


Figure 15. The separation location from the skin friction versus from the K_s method. The shaded band indicates ±15% about the $y = x$ line.

This fit was geometry-dependent, as it was calibrated for the *SPLEEN C1* cascade only, and it should not be assumed applicable to other blade geometries without recalibration.

Figure 16 shows the acceleration parameter at separation versus the surface-length Reynolds number. The lines result from the correlation of Hatman and Wang [35], and the lines from Michalek et al. [36] were added for completeness. Agreement with the Hatman and Wang correlation [35] improved significantly after applying the above correction, particularly for $M \leq 0.90$ and $Re > 100{,}000$. Cases at $M = 0.95$ followed the same trend but departed due to the shock–boundary layer interaction [18,33].

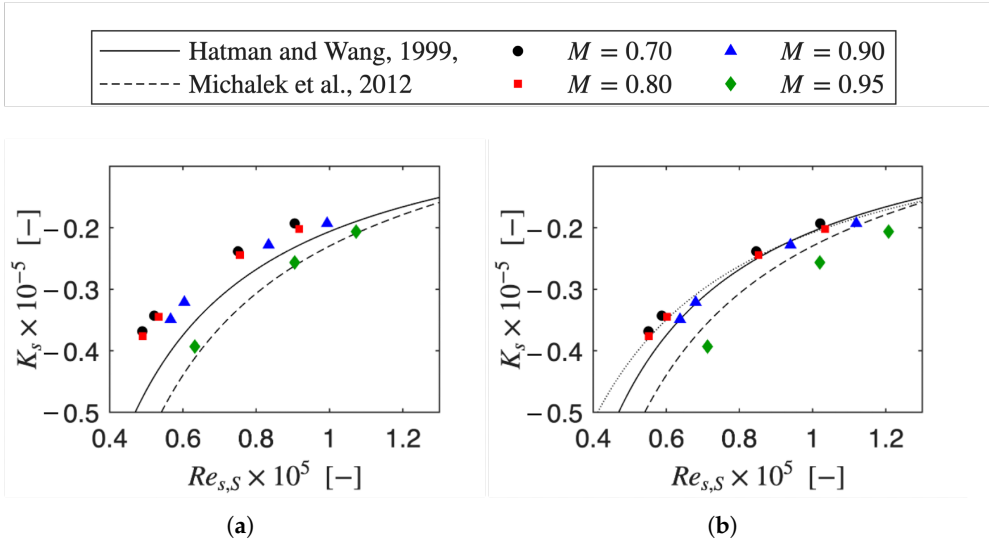


Figure 16. The acceleration parameter at separation versus the surface-length-based Reynolds number: without correction (**a**) and with separation-location correction (**b**). Correlations of Hatman and Wang [35], and Michalek et al. [36] are included for comparison.

The relation between the Reynolds numbers at reattachment and separation is given in Figure 17. Experimental points fell within the envelope of existing correlations [35–37]. The lower-Mach number cases aligned closely with Hatman and Wang, and the lowest-Mach number cases trended toward Houtermans.

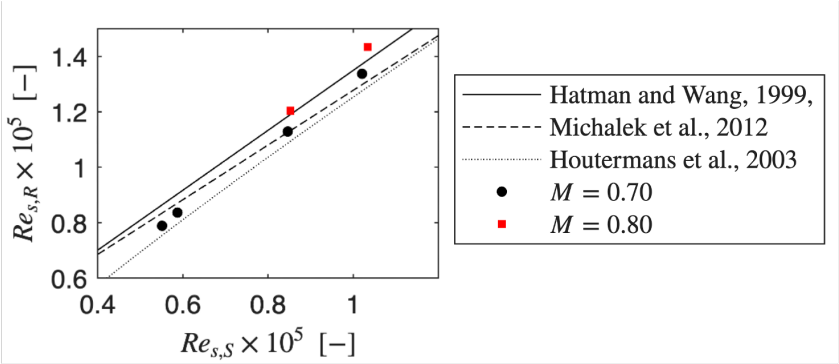


Figure 17. The surface-length-based Reynolds number at reattachment versus at separation. Correlations of Hatman and Wang [35], Michalek et al. [36], and Houtermans et al. [37] are included for comparison.

Tables 7 and 8 summarize the separation and reattachment locations from experiments and numerical results. For the K_s method, premature separation of about 1.5% of the surface length appeared at a lower Mach number. At $M = 0.90$ and $Re = 120{,}000$, the separation location was underpredicted by ≈2.9%. The largest CFD–experiment discrepancy occurred at $M = 0.95$ (up to 8%). Away from shock interaction, CFD tended to delay separation by up to ∼3.4%. MISES usually predicted later separation by up to ∼4%, except at $M = 0.70$, where earlier separation by ∼1% was obtained. Reattachment from CFD was delayed at $Re = 65{,}000$ and 70,000 (up to 5.5%) and was premature at higher Re, implying a shorter bubble than measured. MISES underpredicted reattachment by ∼9% across conditions.

These outcomes indicate that classical separated-induced transition behavior was largely preserved up to $M \leq 0.90$, for which there were no strong passage shocks. Accuracy deteriorated when the shock–boundary layer interaction became dominant at $M = 0.95$.

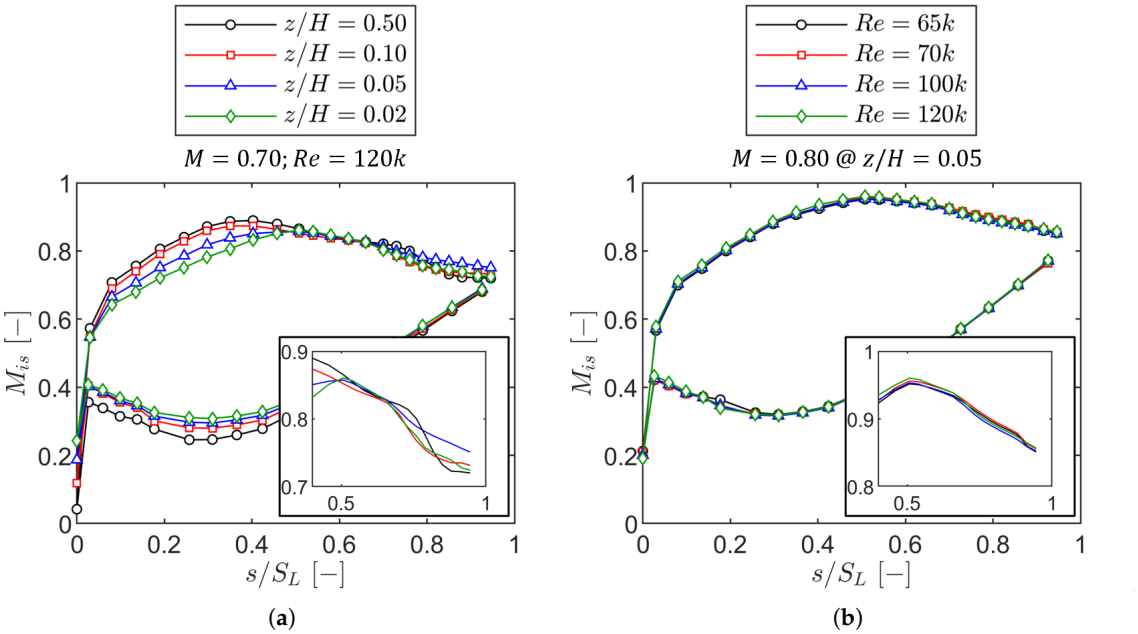
Table 7. The separation location, s_{sep}/S, from the experiments, CFD, and MISES under steady inlet flow.

		Exp.						
		from K_s	from τ_q	ϵ [%]	CFD	ϵ [%]	MISES	ϵ [%]
65,000	0.70	0.612	-	-	0.614	0.21	0.619	0.68
	0.80	0.637	-	-	0.669	3.17	0.681	4.41
	0.90	0.747	-	-	0.730	−1.67	-	-
70,000	0.70	0.610	0.601	−1.53	0.614	0.42	0.619	0.89
	0.80	0.637			0.662	2.49	0.676	3.84
	0.90	0.741	0.752	1.55	0.723	−1.73	-	-
100,000	0.70	0.612	-	-	0.601	−1.15	0.602	−1.00
	0.80	0.635	-	-	0.669	3.37	0.676	4.04
	0.90	0.716	-	-	0.703	−1.29	0.756	3.99
120,000	0.70	0.610	0.601	−1.53	0.614	0.42	0.602	−0.79
	0.80	0.637	-	-	0.662	2.49	0.670	3.27
	0.90	0.712	0.691	−2.89	0.723	1.16	0.733	2.10

Table 8. The reattachment location, s_{reatt}/S, from the experiments, CFD, and MISES.

		Exp.						
		from K_s	**from τ_q**	**ϵ [%]**	**CFD**	**ϵ [%]**	**MISES**	**ϵ [%]**
65,000	0.70	0.931	-	-	0.985	5.46	0.848	−8.23
70,000	0.70	0.921	-	-	0.972	5.12	0.837	−8.45
100,000	0.70	0.871	-	-	0.852	−1.84	0.802	−6.86
	0.80	0.932	-	-	0.915	−1.75	0.854	−7.86
120,000	0.70	0.858	0.873	1.800	0.771	−8.68	0.773	−8.44
	0.80	0.921	-	-	0.845	−7.58	0.831	−9.05

The spanwise variation was assessed using the traversable blade. The blade loading decreased toward the endwall for all cases. Figure 18a shows the progressive reduction at $M = 0.70$ and $Re = 120{,}000$. The zoomed region highlights a shorter suction side separation bubble that was near the endwall, primarily attributable to the secondary flow transport along the suction side, which locally suppressed the separation in the secondary flow penetration region [16]. At a fixed Mach number, the near-wall loading in the secondary flow region was largely insensitive to Re. An example at $M = 0.80$ is given in Figure 18b.



(**a**) (**b**)

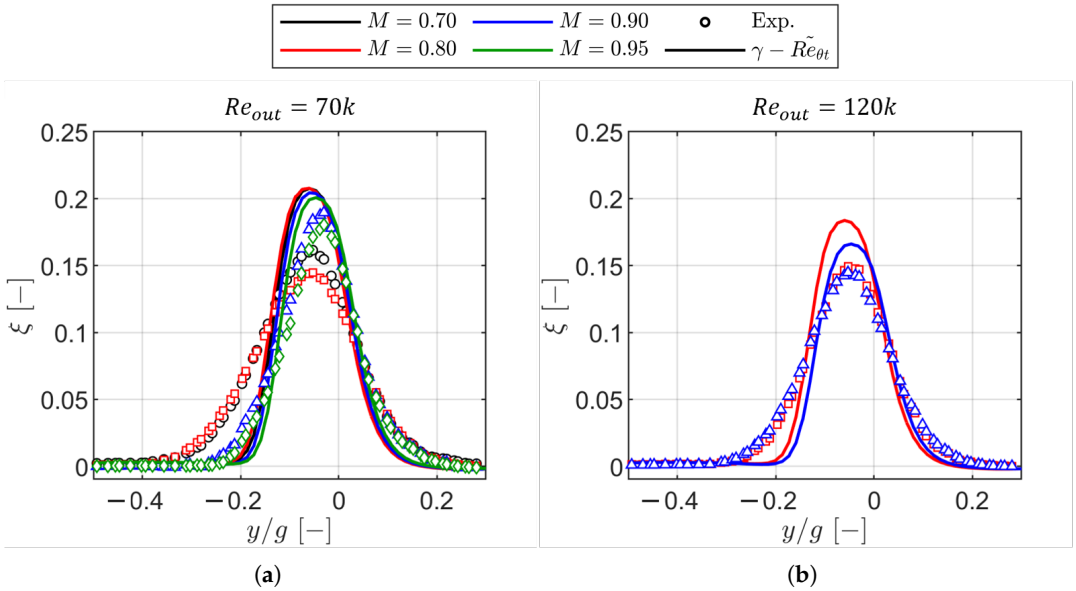
Figure 18. The spanwise variation of the blade loading: $M = 0.70$, $Re = 120{,}000$ (**a**) and the sensitivity of the near-wall loading at $z/H = 0.05$ to the Reynolds number at $M = 0.80$ (**b**).

4.4. Profile Wake and Loss

The blade wake was characterized from the pitchwise distribution of the kinetic energy loss coefficient at Plane 06. The coefficient was computed using the inlet freestream total pressure, the local outlet total pressure, and the endwall static pressure from the Plane 06 taps. Wakes for $Re = 70{,}000$ and $Re = 120{,}000$ are shown in Figure 19a,b.

At $Re = 70{,}000$, RANS underestimated the wake depth and showed little variation in the wake width across the Mach number. The widest experimental wake occurred at $M = 0.80$, which is consistent with the open separation thickening the suction side boundary layer. As the Mach number increased, the separation shifted aft, shortening the development length and thinning the wake; by $M = 0.95$, the RANS wake depth approached the measured values. At $Re = 120{,}000$, RANS predicted reattachment for both Mach numbers, yielding a thinner boundary layer and a narrower wake at $M = 0.90$.

The measurements only indicate reattachment at the lowest Mach number. However, the wakes converged at higher Mach numbers due to the stronger acceleration and thinner boundary layer.



(**a**) (**b**)

Figure 19. The pitchwise distribution of the kinetic energy loss coefficient: Re = 70k (**a**) and Re = 120k (**b**).

Figure 20 reports the mass-averaged kinetic energy loss. At the lowest Reynolds number, both the measurements and RANS monotonically decreased with the Mach number. The measured loss dropped by about 23% from $M = 0.70$ to 0.95, while RANS showed a reduction of about 9%, and it typically underpredicted the loss except at $M = 0.95$. Increasing the Reynolds number reduced the loss. Suppressing the open separation at $M = 0.80$ lowered the loss by about 19%. In the measurements, the loss plateaued at the highest Reynolds number. The loss obtained with RANS continued to decrease.

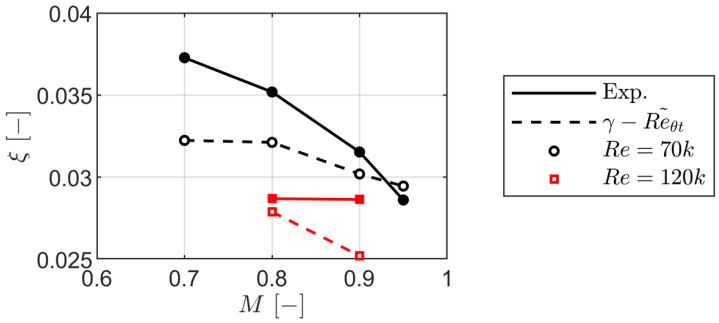


Figure 20. The mass-averaged profile loss in terms of the kinetic energy loss coefficient.

4.5. Secondary Flows

The primary flow structures were briefly characterized to support the measurements at the cascade outlet. A 3D transitional RANS simulation, supplied with experimentally measured inlet boundary conditions (radial distributions of the total pressure, incidence, turbulent quantities, and outlet static pressure), was qualitatively used to identify the likely structures. A detailed setup was omitted because the work is part of an ongoing collaboration. The results are qualitatively used as guidance.

Figure 21 shows the Q-criterion at $M = 0.90$, $Re = 70{,}000$, with iso-surfaces colored by axial vorticity. The dominant structure is the passage vortex (PV, green) system. The two co-rotating structures visible in the Q-criterion visualization are part of the same passage

vortex system. Their apparent separation depends on the chosen Q-criterion iso-level and does not indicate distinct passage vortices. Inspection of the vorticity and secondary velocity vectors confirmed a single-passage vortex system. Above the passage vortex, a wall-induced vortex (WIV) of an opposite sign developed and remained attached to the suction side. Reduced blade loading near the endwall generated a counter vorticity region that fed the trailing shed vorticity (TSV), while a corner vortex (CV) formed at the suction side/endwall junction.

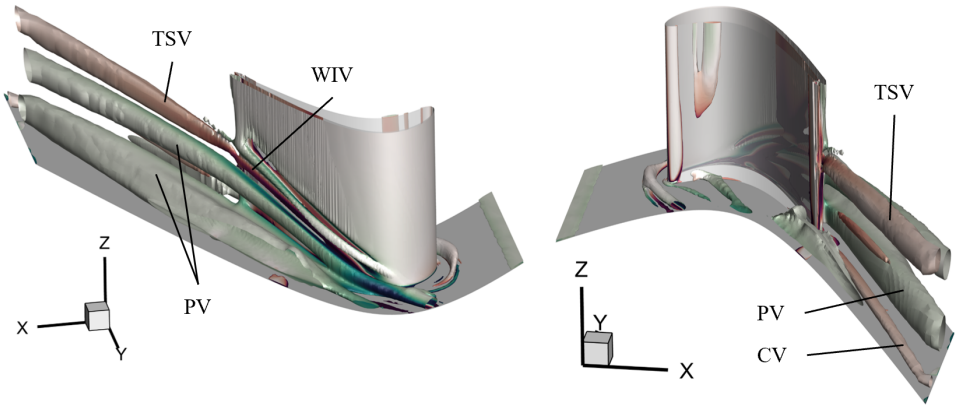


Figure 21. Representation of the primary and secondary flow structures with the Q-criterion.

The outlet secondary field at Plane 06 was mapped with the L-shaped five-hole probe. Three quantities were used to describe location and strength, i.e., the kinetic energy loss coefficient ξ, the streamwise vorticity coefficient K_ω, and the secondary kinetic energy coefficient K_{SKE}:

$$\xi = 1 - \frac{1 - \left(\frac{P_6}{P_{06}}\right)^{\frac{\gamma-1}{\gamma}}}{1 - \left(\frac{P_6}{P_{01}}\right)^{\frac{\gamma-1}{\gamma}}}, \tag{7}$$

$$K_\omega = \frac{C}{V_{6,is}}(\omega_{ax} cos\beta_{MS} + \omega_{tan} sin\beta_{MS}), \tag{8}$$

$$K_{SKE} = \frac{\rho_6\left(v_{y,sec}^2 + v_{z,sec}^2\right)}{\gamma P_6 M_{6,is}^2}, \tag{9}$$

with $v_{y,sec} = V_{tan}\cos\beta - V_{ax}\sin\beta$ and $v_{z,sec} = V_{rad}$. The axial and tangential vorticity were computed as:

$$\omega_{ax} = \frac{\partial V_{rad}}{\partial y} - \frac{\partial V_{tan}}{\partial z}, \tag{10}$$

$$\omega_{tan} = \frac{1}{V_{ax}}\left(V_{tan}\omega_{ax} + \frac{a^2}{\gamma}\frac{\partial(lnP_{06})}{\partial z}\right). \tag{11}$$

Figure 22 illustrates the nominal case. In Figure 22a, ξ shows a midspan wake and two endwall loss cores. Core "C1" lay above $z/H \approx 0.10$ and was shifted from the trailing edge metal-angle line ($y/g = 0$). Core "C2" sat close to the endwall and followed the outlet metal angle. Figure 22b overlays K_ω on ξ. The clockwise vorticity near the endwall corresponded to the CV and aligned with "C2." A second clockwise region around $z/H \approx 0.10$ was influenced by TSV. The counter-clockwise vorticity on the adjacent pressure side marks the PV, whose interaction with TSV contributed to "C1." Figure 22c shows K_{SKE} with secondary velocity vectors. High K_{SKE} appeared at interfaces between structures and the endwall, with the largest values being where PV and TSV interacted.

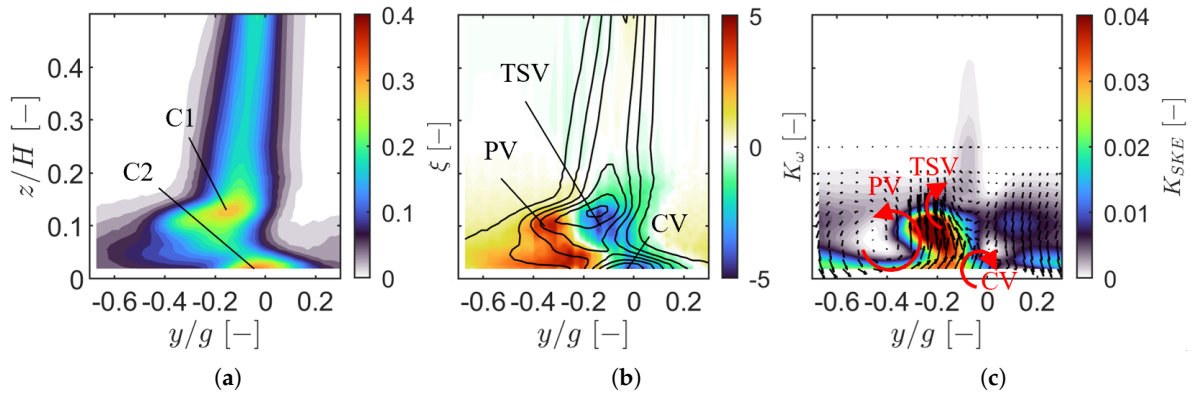


Figure 22. The secondary flow structures at Plane 06 for the nominal flow case: the kinetic energy loss coefficient (**a**), the streamwise vorticity coefficient superimposed with isolines of the kinetic energy loss coefficient (**b**), and the secondary kinetic energy coefficient superimposed with the secondary velocity vectors (**c**). The observer looked upstream.

At fixed Re = 70,000, increasing the Mach number moveed "C1" toward the endwall and skewed the wake near the endwall (Figure 23). This migration with the Mach number agreed with prior cascade investigations, such as [9–11,13].

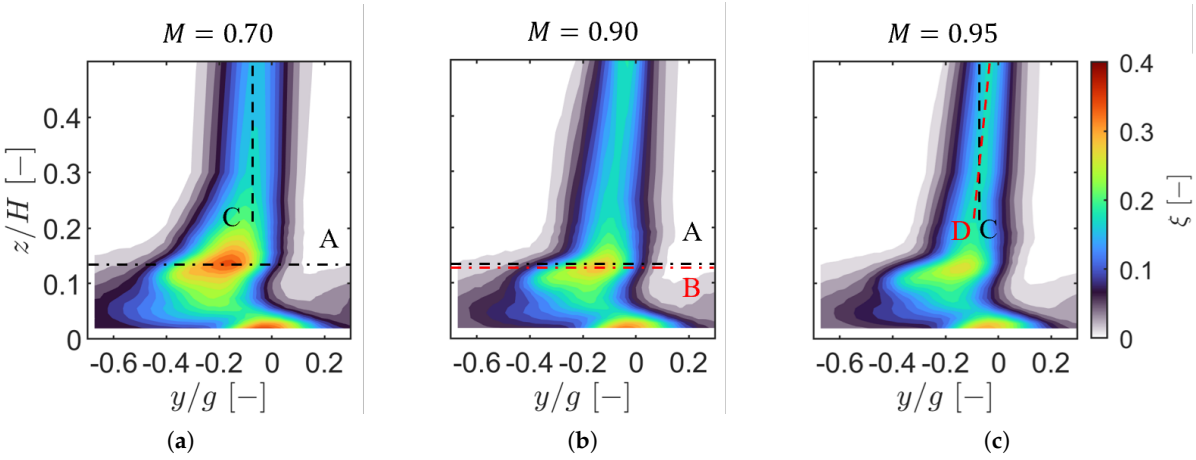


Figure 23. Impact of the Mach number at a Reynolds number of 70,000: M = 0.70 (**a**), M = 0.90 (**b**), and M = 0.95 (**c**).

The spanwise, mass-averaged ξ_{sec} (gross loss minus profile and inlet–BL contributions) is plotted in Figure 24a. Two peaks were evident: one associated with PV+TSV ("C1"), and a larger one combining CV and the endwall boundary layer. As the Mach number increased, the overall ξ_{sec} decreased and the "C1" peak dropped by about 25%. The mass-averaged radial flow deviation (Figure 24b) showed underturning and overturning near the endwall. The peak underturning weakened by about 9% with an increasing Mach number, consistent with weaker secondary structures. The secondary kinetic energy loss S_{SKE} (Figure 24c) highlighted two zones: Region "A" near the endwall from CV and endwall BL, and Region "B" at the PV–TSV shear. The "B" peak varied less with the Mach number than ξ_{sec} but was still reduced by roughly 7%.

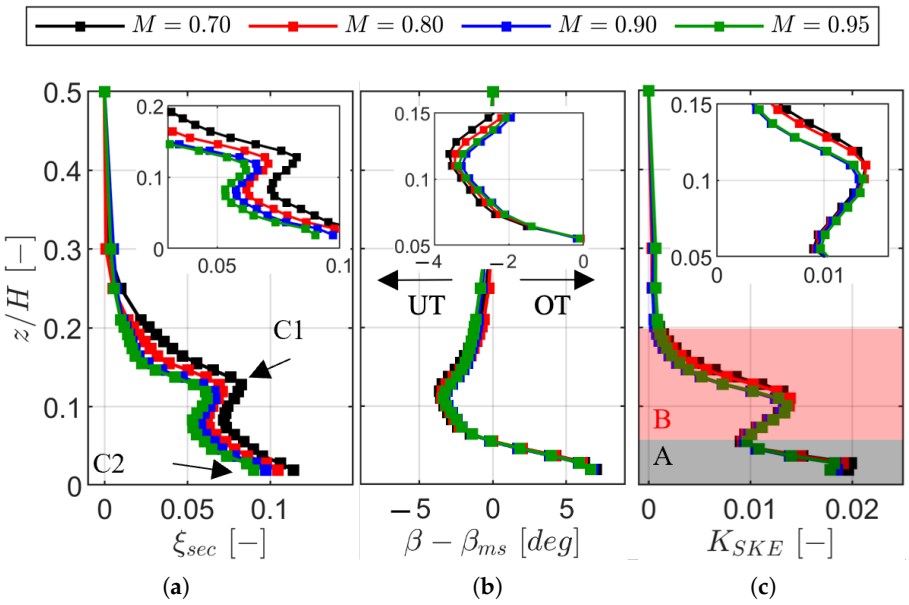


Figure 24. The radial profiles for Re = 70k: the secondary kinetic energy loss coefficient (**a**), the deviation from the primary flow direction (**b**), and the secondary kinetic energy coefficient (**c**).

The Reynolds number effects at $M = 0.90$ are shown in Figure 25. Increasing the Reynolds number reduced the magnitude below "C1," giving an ~11% drop in the "C1" peak of ξ_{sec} (Figure 25a). In contrast, the underturning in the PV region intensified with the Reynolds number (Figure 25b), and the dominant K_{SKE} core increased by ~13% (Figure 25c). The differing trends of ξ_{sec} and K_{SKE} suggest that ξ_{sec} may have retained some sensitivity to the inlet BL contributions despite the subtraction.

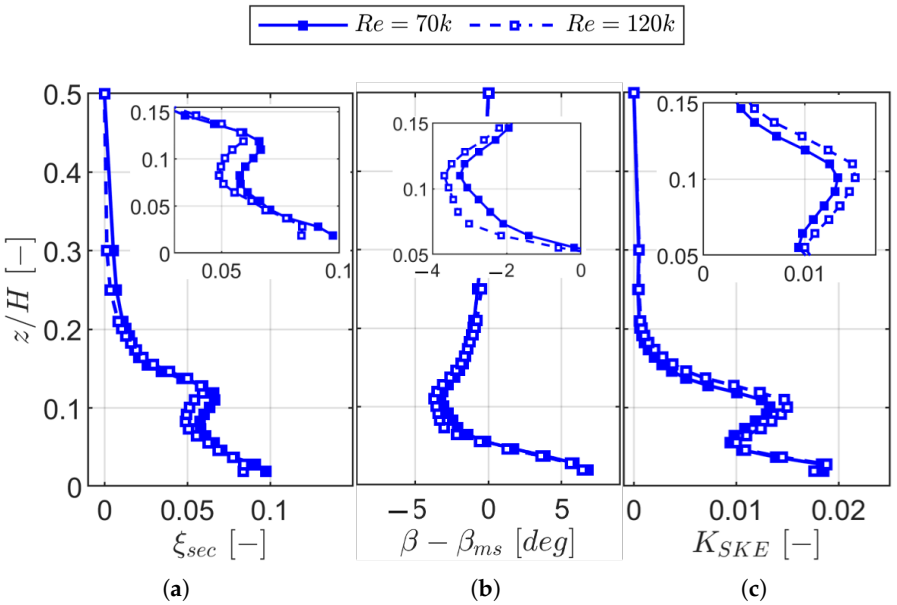


Figure 25. The radial profiles for M = 0.90: the secondary kinetic energy loss coefficient (**a**), the deviation from the primary flow direction (**b**), and the secondary kinetic energy coefficient (**c**).

A planewise loss breakdown is provided in Figure 26. The net loss was defined as

$$\xi_{net} = \xi_{gross} - \xi_{prof} - \xi_{BL}. \quad (12)$$

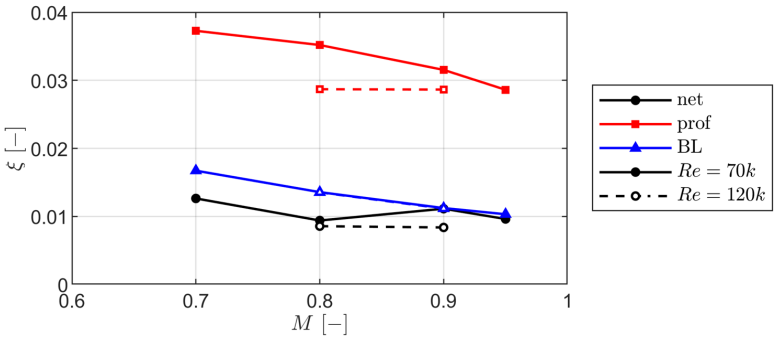


Figure 26. Breakdown of the planewise mass-averaged loss for the steady inlet flow cases.

The inlet boundary layer contribution was essentially independent of the Reynolds number. Profile loss was the largest term, exceeding the endwall contribution by a factor of more than two. It decreased with an increasing off-design Mach number as the suction side separation moved aft and the boundary layer at the trailing edge thinned, and it also decreased with the Reynolds number as the laminar separation bubble shortened. The endwall loss generally diminished with the Mach and Reynolds numbers; for $Re = 70{,}000$, it fell by about 25% between $M = 0.70$ and 0.95, with a minimum near $M = 0.80$. These behaviors are consistent with the linear-cascade findings in the literature, such as [12].

4.6. Loss Modeling

4.6.1. Profile Loss

The profile loss estimates in the literature are mostly geometry-based and trace back to the model of Ainley and Mathieson [38]. Subsequent variants have incorporated features of modern blading [39–43]. Alternative approaches include the models of Craig and Cox [44] and Traupel [45]. A comprehensive comparison for *SPLEEN C1* is given in [18].

A limitation of these classical models is the lack of a clear separation of the constituent loss terms. The formulation of Senior and Miller [46] overcomes this, provided a blade loading is available. The model includes recent trailing edge loss physics following Melzer and Pullan [47] and Rossiter et al. [48]:

$$\xi = \frac{2\sum\theta}{g\cos\alpha_{out}}\left(\frac{V_{TE,SS}}{V_{out}}\right)^2 + \left(\frac{t_{TE}+\sum\delta^*_{TE}}{g\cos\alpha_{out}}\right)\frac{V_{TE,SS}}{V_{out}}\left(\frac{V_{TE,SS}}{V_{out}}\cos\frac{\alpha_w}{2} - 1\right) + \left(\frac{t_{TE}+\sum\delta^*}{g\cos\alpha_{out}}\right)\left(\frac{V_{TE,SS}}{V_{out}}\right)^2 \sin\frac{\alpha_w}{2} - C^*_{pb}\left(\frac{t_{TE}+\sum\delta^*_{TE}}{g\cos\alpha_{out}}\right)\left(\frac{V_{TE,SS}}{V_{out}}\right)^2, \quad (13)$$

where the base–pressure coefficient is

$$C^*_{pb} = \frac{P_{base} - P_{TE,SS}}{\frac{1}{2}\rho V^2_{TE,SS}}. \quad (14)$$

Boundary layer integral quantities near the trailing edge were estimated using the model of Coull and Hodson [27]. The pressure side boundary layer was assumed attached, even though RANS and MISES captured a small laminar separation bubble in the experiments. The Coull–Hodson correlations account for growth in the presence of a laminar separation bubble, separating contributions from the bubble and the downstream turbulent development:

$$[\theta_{SS,TE}]_{bubble} = \theta_{SS,sep}\left(6.69\times10^6\right)\left(Re_{\theta,sep}\right)^{(-4.28+2.05(\Delta U^*/\Delta S^*)-0.16St)}, \quad (15)$$

$$[\theta_{SS,TE}]_{turb} = \theta_{SS,sep}\left(Re_{\theta\,sep}\right)^{0.322}\left(\frac{1-s_{sep}}{S_L}\right)\left(0.166+3.13\left(\frac{\Delta U^*}{\Delta S^*}\right)\right). \quad (16)$$

The total momentum thickness was computed as the sum of contributions:

$$[\theta_{SS,TE}] = [\theta_{SS,TE}]_{bubble} + [\theta_{SS,TE}]_{turb}. \quad (17)$$

Estimating the separation location was required to evaluate the growth across the bubble. Two families of methods were examined: the Thwaites-parameter criteria (Equation (18)) and the Stratford-type criteria (Equation (19)).

$$[\lambda_\theta]_{sep} = \left[\frac{\theta^2}{\nu}\frac{dU}{dS}\right]_{sep} \approx const. \quad (18)$$

$$\left[C_p^*\left((S-S_B)\frac{dC_p^*}{dS}\right)\right]_{sep} \approx const. \quad (19)$$

The constants adopted for common Thwaites-based variants are listed in Table 9.

Table 9. Constants for the Thwaites-parameter separation criteria.

Model	Const.
Pohlhausen [49]	−0.1567
Timman [50]	−0.0871
Walz [51]	−0.0682
Thwaites [52]	−0.0820
Curle and Skan [53]	−0.0900

In Stratford's method, the constant depends on an m coefficient used to describe the boundary layer inner layer, and S_B is a leading edge correction used when the velocity does not remain flat up to the peak:

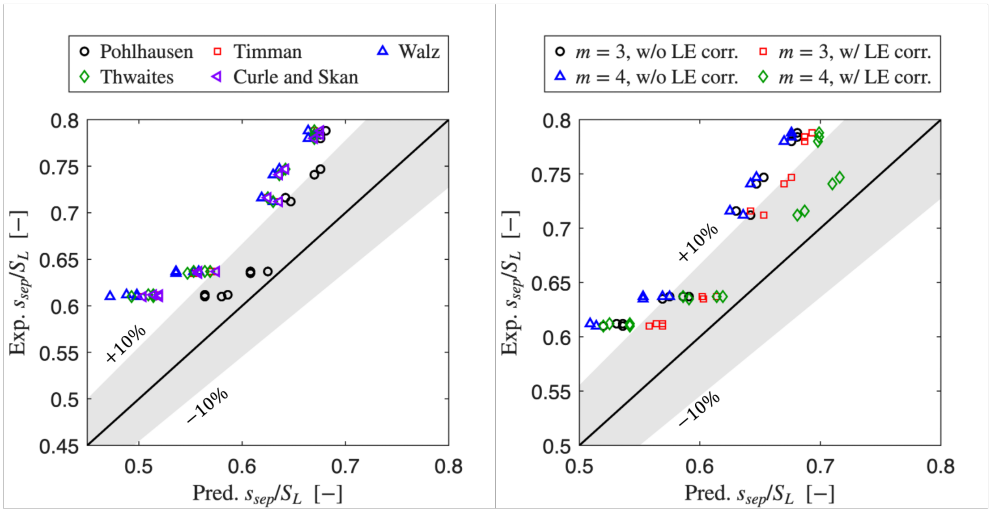
$$S_B = S_{peak} - \int_0^{S_{peak}}\left(\frac{V}{V_{peak}}\right)^5 dS. \quad (20)$$

The adopted constants for the Stratford-type criteria are given in Table 10.

Table 10. Constants for the Stratford-type separation criteria.

Model	Const.
Stratford [54], $m = 3$	0.0108
Stratford [54], $m = 4$	6.48×10^{-3}

Fully turbulent blade loadings from MISES were used as input for the separation prediction. Across the present cases, the difference in predicted profile loss when using RANS instead of MISES remained within ±1%. Figure 27 compares the experimentally inferred separation locations with predictions. Among the Thwaites-type criteria, the Pohlhausen variant provided the smallest error, typically within ±10% (Figure 27a). For the Stratford-type criteria, the minimum error occurred for $m = 3$ with the leading edge correction (Figure 27b).



(**a**) (**b**)

Figure 27. Comparison of the experimentally obtained separation locations against those estimated with different methods: Thwaites (**a**) and Stratford (**b**).

As discussed by Coull and Hodson [27], cases with moderate deceleration ($U_{sep}/U_{peak} > 0.935$) are best represented by $m = 3$. All *SPLEEN C1* conditions satisfy this. At a Mach number of 0.70, the velocity ratio is 0.95, increasing as the Mach number rises. Table 11 lists the relevant loading parameters.

Table 11. Summary of the blade loading parameters.

M [−]	Re [−]	U_{sep}/U_{peak} [−]	DF [−]	$\Delta U^*/\Delta S$ [−]	Z_w [−]
0.70	65,000	0.95	25	0.35	0.82
0.80	65,000	0.95	20	0.33	0.78
0.90	65,000	0.95	18	0.35	0.73
0.70	70,000	0.94	25	0.35	0.82
0.80	70,000	0.95	21	0.34	0.78
0.90	70,000	0.97	18	0.37	0.73
0.95	70,000	0.98	16	0.39	0.71
0.70	100,000	0.95	24	0.34	0.81
0.80	100,000	0.97	20	0.35	0.77
0.90	100,000	0.99	16	0.36	0.73
0.95	100,000	0.98	17	0.40	0.71
0.70	120,000	0.95	24	0.35	0.81
0.80	120,000	0.97	21	0.36	0.77
0.90	120,000	0.98	17	0.36	0.73
0.95	120,000	0.98	16	0.38	0.70

Mean absolute errors in separation location are summarized in Table 12. All methods tend to underpredict the separation point. The lowest mean error among Thwaites-type criteria is from the Pohlhausen variant (7.8%). For Stratford-type criteria, $m = 3$ with the leading edge correction gives 8.1%.

Table 12. The mean error in estimating the separation location.

Model	Mean Error [−]
Pohlhausen [49]	−7.8
Timman [50]	−13.6
Walz [51]	−15.8
Thwaites [52]	−14.2
Curle and Skan [53]	−13.4
Stratford [54], $m = 3$, w/o LE corr.	−11.7
Stratford [54], $m = 4$, w/o LE corr.	−13.8
Stratford [54], $m = 3$, w/LE corr.	−8.1
Stratford [54], $m = 4$, w/LE corr.	−8.2

Although the Pohlhausen method showed a lower mean error, the Stratford method offered advantages in specific cases. Figure 28 compares the experimentally inferred separation location with the predictions from the best-performing Thwaites- and Stratford-type criteria. The figure highlights the effect of the Mach number in delaying the separation location. The shaded band represents an error range of ±10%.

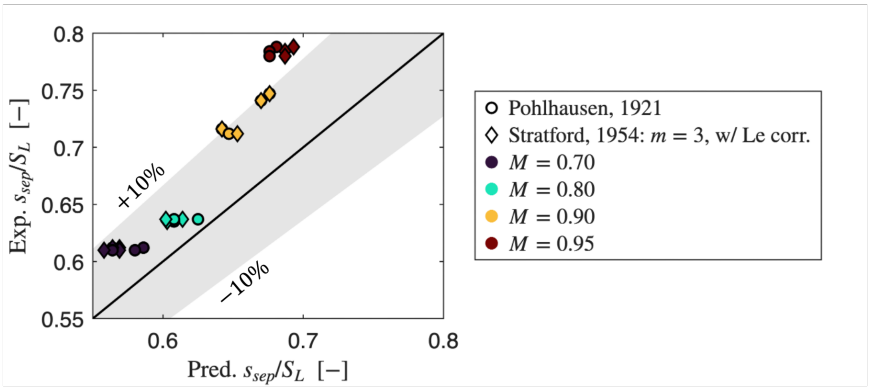


Figure 28. Comparison of the experimentally obtained separation location against the one estimated with the best method of the Thwaites [52] and Stratford [54] type methods.

Agreement of the Pohlhausen method deteriorated at higher Mach numbers when compared with the Stratford method. Table 13 reports the mean error by Mach number set. Based on this evidence, the Stratford criterion with $m = 3$ and a leading edge correction was adopted for the present analysis.

Table 13. The mean error in estimating the separation location for each Mach number for the Pohlhausen and Stratford criteria.

M [−]	Pohlhausen	Stratford, $m = 3$, w/LE corr.
0.70	−6.2	−7.5
0.80	−3.1	−4.5
0.90	−9.7	−9.5
0.95	−13.6	−12.1

Figure 29a compares the experimental and predicted profile loss. The model captured the reduction in profile loss with an increasing Mach number. The model also reproduced the reduction with an increasing Reynolds number. The largest overprediction occurred at a Mach number of 0.70 and a Reynolds number of 65,000, with an error of approximately 7% relative to the experiment.

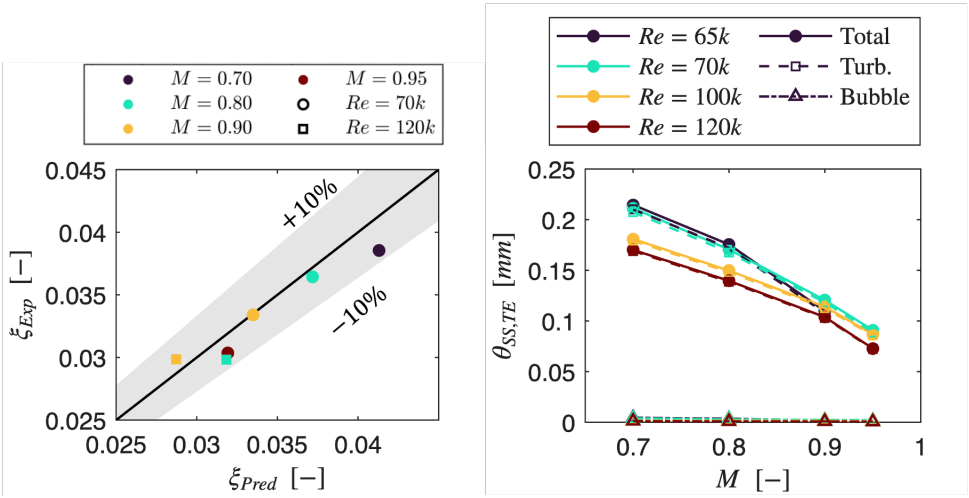


Figure 29. Loss breakdown by flow condition (**a**), and the contributions of BL on SS (**b**) for steady inlet flow cases.

The pressure side displacement thickness was, at most, 40% of the suction side value. Using the Coull and Hodson framework [27], the suction side momentum thickness $\theta_{SS,TE}$ was decomposed. Figure 29b shows the contributions to $\theta_{SS,TE}$ as functions of the Mach number, with the curve color indicating the Reynolds number. The total $\theta_{SS,TE}$ followed the profile loss trend. Turbulent growth contributed up to ∼99%, while the bubble term diminished with increasing Mach and Reynolds numbers.

Recalling the model of Senior and Miller, the profile loss partitioned into boundary layer mixing, as well as blockage-induced, trailing edge wedge angle, and base pressure contributions:

$$\zeta_{mixing} = \frac{2\sum\theta}{g\cos\alpha_{out}}\left(\frac{V_{TE,SS}}{V_{out}}\right)^2, \tag{21}$$

$$\zeta_{blockage} = \left(\frac{t_{TE}+\sum\delta^*_{TE}}{g\cos\alpha_{out}}\right)\frac{V_{TE,SS}}{V_{out}}\left(\frac{V_{TE,SS}}{V_{out}}\cos\frac{\alpha_w}{2}-1\right), \tag{22}$$

$$\zeta_{wedge} = \left(\frac{t_{TE}+\sum\delta^*}{g\cos\alpha_{out}}\right)\left(\frac{V_{TE,SS}}{V_{out}}\right)^2\sin\frac{\alpha_w}{2}, \tag{23}$$

$$\zeta_{base} = C^*_{pb}\left(\frac{t_{TE}+\sum\delta^*_{TE}}{g\cos\alpha_{out}}\right)\left(\frac{V_{TE,SS}}{V_{out}}\right)^2, \tag{24}$$

where C^*_{pb} is the base pressure coefficient and is computed as:

$$C^*_{pb} = \frac{P_{base}-P_{TE,SS}}{\frac{1}{2}\rho V^2_{TE,SS}}. \tag{25}$$

Here, P_{base} was taken at the last available pressure taps on the blade pressure and suction surfaces. The term $P_{TE,SS}$ was taken as the local freestream static pressure near the trailing edge on the suction side. Figure 30 summarizes each contribution versus the Mach number, with the line color indicating the Reynolds number.

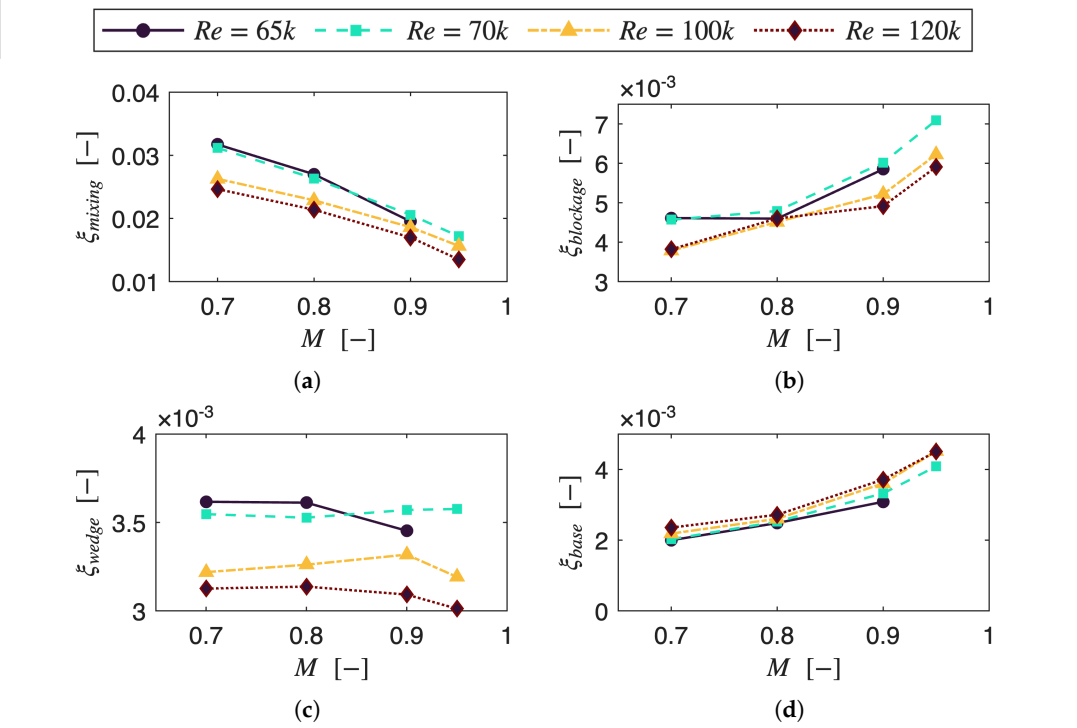


Figure 30. Breakdown of the loss contributions of the profile loss from Equations (21)–(24): the mixing loss (**a**), blockage loss (**b**), trailing edge wedge angle loss (**c**), and base pressure loss (**d**).

The mixing term (Figure 30a) mirrors the overall loss decrease with an increasing Mach number and Reynolds number through the reduction in the boundary layer momentum thickness in Equation (21). The blockage term (Figure 30b) increased with the Mach number. Although displacement thickness contributed, the dominant driver was the velocity ratio $V_{TE,SS}/V_{out}$, which grew as the blade loading reduced. This term accounted for roughly 90% of the total blockage contribution. The trailing edge wedge term (Figure 30c) was nearly invariant with the Mach number, as expected for an effect governed primarily by the fixed wedge angle. A mild decrease with the Reynolds number arose from the thinner trailing edge boundary layers. The base pressure term (Figure 30d) mainly increased with the Mach number. The Reynolds number trend reflected competing changes in the displacement thickness, base pressure coefficient, and velocity ratio.

4.6.2. Secondary Loss

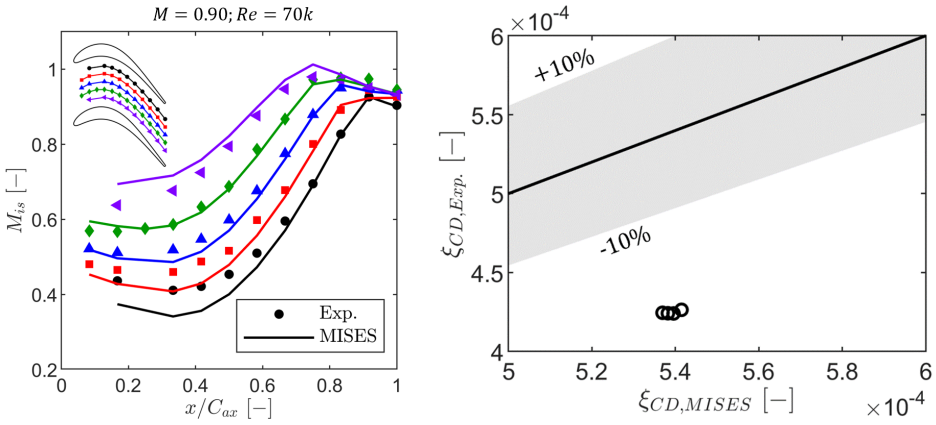
Classical secondary loss correlations (Ainley–Mathieson family [38,39,41–44] and Craig–Cox [44]) were assessed and found to overpredict the loss by up to 600%. A detailed root-cause analysis was beyond the scope here, and these models did not decompose the contributing mechanisms. A comprehensive comparison is provided in [18].

The model of Coull [55] was adopted to separate the contributions of the passage vortex, trailing shed vorticity, and corner vortex. From [55], the endwall loss due to boundary layer dissipation can be approximated as:

$$\zeta_{CD} \approx 2C_D \left(\frac{A_{end}}{Hg\cos\alpha_{out}}\right) \int \left(\frac{T_{out}}{T_{end}}\right)\left(\frac{\rho_{end}}{\rho_{out}}\right)\left(\frac{V_{end}}{V_{out}}\right)^3 d\left(\frac{A}{A_{end}}\right), \tag{26}$$

with a boundary layer dissipation coefficient $C_D \approx 0.02$ [56]. Midspan flowfields from fully turbulent MISES were used to estimate ζ_{CD}, and a like-for-like comparison against endwall measurements was performed to quantify the impact.

Figure 31a shows the isentropic Mach number along the normalized axial direction at the endwall. MISES tended to overpredict near the pressure side and underpredict near the suction side. The resulting symmetry reduced the difference between the integrals evaluated with the endwall data versus MISES quantities. The integral in Equation (26) was evaluated over the endwall area covered by the available taps. Figure 31b compares the resulting endwall loss integrals. Using experimental versus MISES inputs changed the estimate by about 27%, which corresponded to an absolute difference of ∼0.01% (about 5% of the expected endwall loss). The MISES-based approach was, therefore, adequate for the present purposes, and the whole domain from Plane 01 to Plane 06 (i.e., $x/C_{ax} \in [-1.12, 1.50]$) was used.



(**a**) (**b**)

Figure 31. The isentropic Mach number along the normalized axial direction (**a**) and the endwall–loss integral using experimental versus MISES inputs (**b**). The loss integral was evaluated over the experimentally delimited area.

The total endwall loss was written as the sum of endwall dissipation and secondary flow mixing. The latter was modeled via a vorticity amplification framework defined by Coull [55]:

$$\xi_{sec} \approx 0.0021 \times 2M^* \left(\frac{V_{in}}{V_{out}}\right)^2 \left[\frac{\Delta T^*}{g \cos \alpha_{out}} + \frac{\left|\frac{V_{out}}{V_{in}} \sin \alpha_{in} - \sin \alpha_{out}\right|}{\cos \alpha_{out}}\right]. \quad (27)$$

Figure 32 summarizes the sensitivity to the Mach number and the Reynolds number, including the inlet kinetic energy deficit measured at Plane 01. The Mach number trend was captured at both Reynolds numbers. For the lower Reynolds number, all cases lay within ±10% except the case with a Mach number of 0.80. At a higher Reynolds number, the model overpredicted the loss, consistent with its weak Reynolds number sensitivity and with known probe-related challenges in transonic measurements [57,58]. The model also neglected the interaction of the suction and pressure side laminar separation bubbles with the secondary system, which can feed low-momentum fluid into the passage vortex [7].

To characterize the contributions by structure, the amplification factors of Coull were used for the passage vortex, corner vortex, and trailing-shed vorticity:

$$AF_{PV} = \left(\frac{V_{in}}{V_{out}}\right)^2 \left(\frac{\Delta T^* C_{ax}}{g \cos \alpha_{out}} + \frac{\left|\frac{V_{out}}{V_{in}} \sin \alpha_{in} - sin\alpha_{out}\right|}{\cos \alpha_{out}}\right), \quad (28)$$

$$AF_{CV} = -\left(\frac{V_{in}}{V_{out}}\right)^2 \frac{\Delta T^* C_{ax}}{g \cos \alpha_{out}}, \quad (29)$$

$$AF_{TSV} = -\left(\frac{V_{in}}{V_{out}}\right)\frac{\cos\alpha_{in}}{\cos\alpha_{out}}|\tan\alpha_{out} - \tan\alpha_{in}|. \quad (30)$$

Here, M^* is the inlet-to-outlet Mach scaling defined in [55], ΔT^* is the pitchwise inlet total pressure deficit normalized by the outlet dynamic pressure, and $V^* = (1 - \sqrt{1 - (V_1/V_6)^2})$ [59]. The mixing-related secondary loss contribution can then be computed using:

$$\xi_{mix} \approx 0.0021 \sum AF \quad (31)$$

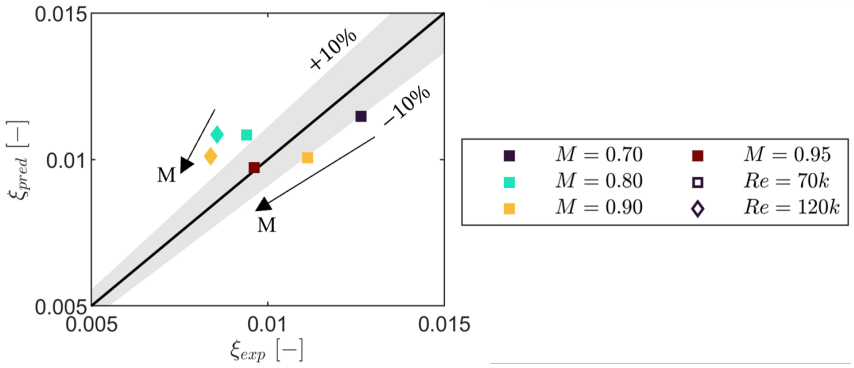


Figure 32. Sensitivity of the endwall loss to the Mach number and the Reynolds number using the model of Coull [55].

Figure 33a shows the amplification factors versus the Mach number for both Reynolds numbers. The passage vortex accounted for roughly 50% of the mixing loss. At lower Mach numbers, the trailing shed vorticity was the second contributor. At higher Mach numbers, the contributions from trailing shed vorticity and the suction side corner vortex became comparable. All contributions decreased with an increasing Mach number and were largely insensitive to the Reynolds number. Figure 33b separates the mixing from endwall dissipation: mixing contributed about 75% of the total endwall loss and decreased with the Mach number. The dissipation part was nearly insensitive to both parameters.

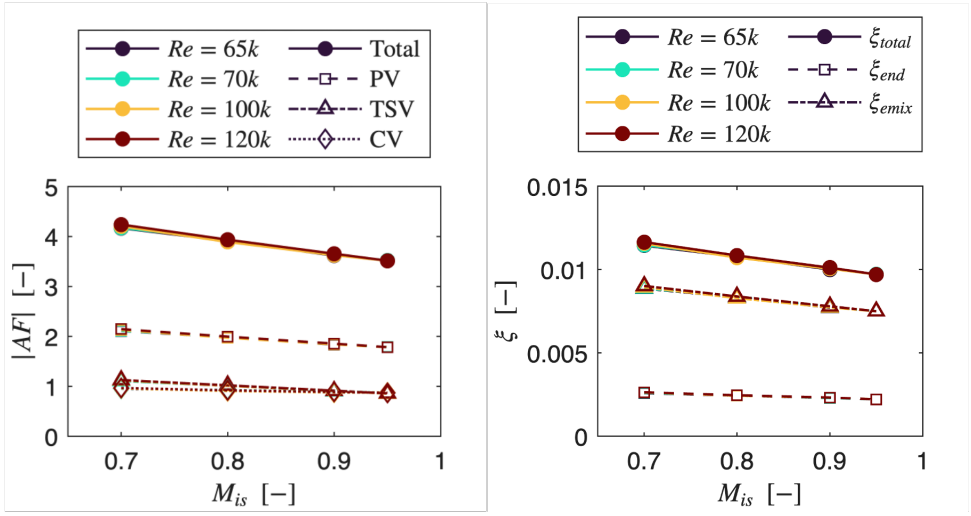


Figure 33. Breakdown by secondary structure (**a**), and the decomposition into endwall dissipation and mixing (**b**) for steady-flow cases.

An alternative model that avoids characterizing the kinetic energy of the inlet boundary layer is the Coull and Clark approach [59]. It uses the inlet boundary layer thickness δ_{98} and shape factor H_{12} via a tabulated parameter

$$\Pi_{SKE} = f\left(\frac{\delta_{98}}{g\cos\alpha_{out}}, H_{12}\right) \tag{32}$$

to predict the secondary kinetic-energy loss coefficient

$$\zeta_{SKE} \approx 2\left(\frac{g\cos\alpha_{out}}{H}\right)\left[\frac{\Gamma_{sec}}{V_{out}g\cos\alpha_{out}}\right]^2 \Pi_{SKE}, \tag{33}$$

where the secondary circulation is

$$\frac{\Gamma_{sec}}{V_{out}g\cos\alpha_{out}} = V^*\frac{\Delta T^* C_{ax}}{g\cos\alpha_{out}} + \left|\frac{V_{in}}{V_{out}}\frac{\sin\alpha_{in}}{\cos\alpha_{out}} - V^*\tan\alpha_{out}\right|. \tag{34}$$

Figure 34 shows the sensitivity of ζ_{SKE} to the Mach number and the Reynolds number using boundary layer parameters from Plane 01. For the lower Reynolds number, the lowest and highest Mach number cases fell outside ±10% by up to 23% at a Mach number of 0.95. At a Mach number of 0.80 and a Reynolds number of 120,000, the loss was underpredicted by about 17%. These discrepancies were consistent with the probe limitations in the transonic fields and with the assumption of the spanwise uniform static pressure at Plane 06 when deriving secondary velocities.

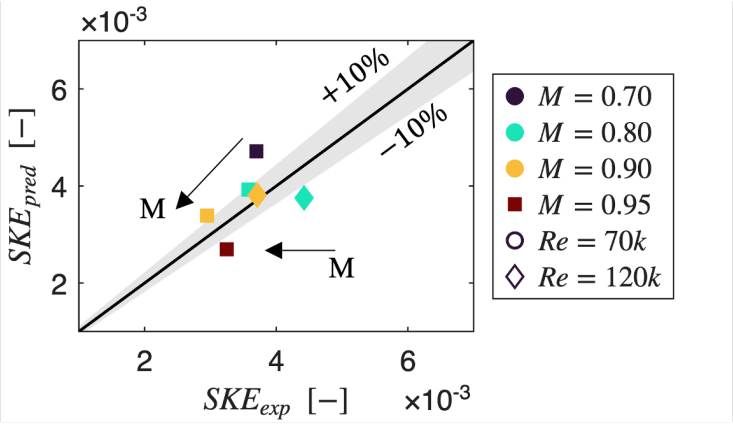


Figure 34. The sensitivity of the secondary kinetic energy to the Mach and Reynolds numbers using the model of Coull [59].

5. Conclusions

This paper analyzed the open *SPLEEN C1* high-speed low-pressure turbine cascade test case under the steady inlet flow over a matrix of operating points spanning $M_{\text{out}} = 0.70$–0.95 and $Re_{\text{out}} = 65{,}000$–$120{,}000$. Experiments were used as the primary reference, with MISES and 2D RANS being employed to support interpretation and to assess the transition and loss modeling in the combined high-Mach, low-Reynolds numbers regime.

At midspan, the dominant mechanism controlling profile loss was suction side separation and transition. As the Mach number increased, separation moved aft and the wake generally thinned. At $M_{\text{out}} = 0.95$, the shock–boundary–layer interaction modified the aft loading and reduced the reliability of the separation indicators and model predictions. Near the endwall, the secondary flow transport along the suction side suppressed the separation within the secondary flow penetration region.

From a modeling perspective, MISES and 2D RANS reproduced the main blade loading trends once the inlet turbulence and transition settings were calibrated. MISES provided

robust and rapid solutions suited to parametric sweeps. 2D RANS provided additional flowfield information but showed reduced reliability for cases with open separation, late reattachment near the trailing edge, and strong shock interaction.

A profile loss breakdown based on the Senior–Miller formulation coupled with the Coull–Hodson boundary layer correlations captured the measured trends when the separation was estimated using a Stratford-type criterion ($m = 3$ with leading-edge correction). Over the present dataset, the coupled model matched the measured profile loss with an RMS error of 4.7%, and the decomposition indicated boundary layer mixing as the dominant contribution.

The outlet secondary field was characterized by a passage vortex system, trailing shed vorticity, and a suction side corner vortex. The Coull vorticity amplification framework captured the Mach number trend of secondary loss and remained within $\pm 10\%$ for most conditions, with larger deviations at higher Reynolds numbers. The Coull–Clark approach predicted secondary kinetic energy within $\pm 10\%$ for most cases using the inlet boundary layer thickness and shape factor, with larger deviations at the lowest and highest Mach numbers.

Author Contributions: Conceptualization, methodology, formal analysis, investigation, data curation, writing—original draft preparation, writing—review and editing: G.L., L.S., A.F.M.T., M.P. and S.L. All authors have read and agreed to the published version of the manuscript.

Funding: This research was funded by the Clean Sky 2 Joint Undertaking under the European Unions Horizon 2020 research and innovation program under the grant agreement 820883.

Data Availability Statement: The data presented in this study are openly available on Zenodo at https://doi.org/10.5281/zenodo.7264761 (accessed on 12 December 2025), reference number [15].

Acknowledgments: The authors gratefully acknowledge the funding of the SPLEEN project by the Clean Sky 2 Joint Undertaking under the European Unions Horizon 2020 research and innovation program under the grant agreement 820883. The authors also acknowledge ASME as the original publisher of the content displayed in this paper, who granted permission to use the material of the following papers presented at ASME Turbo Expo 2022, held in Rotterdam on 13–17 June 2022: *"An Experimental Test Case for Transonic Low-Pressure Turbines–Part I: Rig Design, Instrumentation and Experimental Methodology"* and *"An Experimental Test Case for Transonic Low-Pressure Turbines-Part 2: Cascade Aerodynamics at On- and Off-Design Reynolds and Mach Numbers"*. The authors also acknowledge Nicola Rosafio for providing the 3D RANS data.

Conflicts of Interest: Author Loris Simonassi was employed by the company Avio Aero. Author Antonino Federico Maria Torre was employed by the company MTU Aero Engines. Author Marios Patinios was employed by the company GE Aerospace. The remaining authors declare that the research was conducted in the absence of any commercial or financial relationships that could be construed as a potential conflict of interest.

List of Symbols

Abbreviations

AF	Amplification factor
AP	Aerodynamic probes
BL	Boundary layer
BP	Blade pneumatic taps
CFD	Computational fluid dynamics
CV	Corner vortex
C5HP	Cobra-shaped five-hole probe

DF	Diffusion factor, $(M_{peak} - M_{out})/M_{out}$
EP	Endwall pneumatic taps
ER	Expansion ratio
GTF	Geared turbofan
HF	Surface-mounted hot-films
HS	High speed
ILS	Integral length scale
LE	Leading edge
L5HP	L-shaped five-hole probe
LPT	Low-pressure turbine
OT	Overturning
PS	Pressure side
PT	Boundary layer Preston tube
PV	Passage vortex
RANS	Reynolds-averaged Navier–Stokes
SS	Suction side
SST	Shear-stress transport (turbulence model)
TE	Trailing edge
TG	Turbulence grid
TI	Turbulence intensity
TSV	Trailing shed vorticity
UT	Underturning
WIV	Wall-induced vortex
XW	Cross-wire

Roman

A	Area
C	True chord
C_0	Circulation coefficient $\left(C_0 = \frac{\oint V_s ds}{V_{out} S_L}\right)$
C_p	Pressure coefficient
C^*_{pb}	Base pressure coefficient
C_f	Skin friction coefficient
C_D	Boundary layer dissipation coefficient
g	Cascade pitch
H	Cascade span
H_{12}	Shape factor
inc	Incidence, $\beta - \beta_{in}$
k	Turbulent kinetic energy
K_s	Acceleration parameter
K_{SKE}	Secondary kinetic energy coefficient
K_ω	Streamwise vorticity coefficient
M	Mach number
o	Throat
P	Pressure
Re	Reynolds number, $\rho CV/\mu$
$strm$	Streamlines
s	Curvilinear abscissa along surface
S_L	Surface length
T	Temperature
t_{TE}	Trailing-edge thickness
U, V	Absolute velocity
x, y, z	Location along the axial chord, pitchwise, and spanwise directions

Z_w	Zweiffel coefficient $\left(Z_w = \frac{\oint Pdx}{C_x(P_{0,in} - P_{out})}\right)$
$\Delta U^*/\Delta S$	Non-dimensional deceleration rate
Π_{SKE}	Coull–Clark tabulated parameter
Γ_{sec}	Secondary circulation
ΔT^*	Non-dimensional turning parameter (Coull)
V^*	Coull velocity scaling parameter

Greek letters

α	Angle
α_w	Trailing edge wedge angle
β	Primary flow direction ($\beta = \tan^{-1}(V_{tan}/V_{ax})$)
γ	Ratio of specific heats, cascade pitch angle ($\gamma = \tan^{-1}(V_r/V_{ax})$)
δ_{TE}	Trailing edge thickness
δ_{99}	99% thickness
δ^*	Displacement thickness
ϵ	Dissipation rate, relative error
θ	Momentum thickness
κ	Turbulent kinetic energy
λ_θ	Thwaites parameter
ν	Kinematic viscosity
ζ	Stagger angle
ζ_{SKE}	Secondary kinetic energy loss coefficient
μ	Dynamic viscosity
ρ	Density
ξ	Kinetic energy loss coefficient
τ_q	Quasi-wall shear stress

Subscripts and superscripts

a	Area-averaged
ax	Axial
BL	Boundary layer
CD	Dissipation (endwall)
fs	Freestream
end	Endwall
exp	Experimental
in	Inlet
is	Isentropic
m	Mass-averaged, metallic
mix	Mixing
MS	Midspan
out	Outlet
prof	Profile
PS	Pressure side
S	Separation
sec	Secondary
sep	Separation
SS	Suction side
TE	Trailing edge vicinity
tan	Tangential
tot	Total
turb	Turbulent
R	Reattachment
rad	Radial

Rec	Recovery
0	Flow-off, cold, total
1	At Plane 01
2	At Plane 02
6	At Plane 06

References

1. Kurzke, J. Fundamental Differences Between Conventional and Geared Turbofans. In Proceedings of the ASME Turbo Expo 2009: Power for Land, Sea, and Air, Orlando, FL, USA, 8–12 June 2009; pp. 145–153. [CrossRef]
2. Hodson, H.P.; Howell, R.J. The Role of Transition in High-Lift Low-Pressure Turbines for Aeroengines. *Prog. Aerosp. Sci.* **2005**, *41*, 419–454. [CrossRef]
3. Torre, D.; García-Valdecasas, G.; Puente, A.; Hernández, D.; Luque, S. Design and Testing of a Multi-Stage Intermediate Pressure Turbine for Future Geared Turbofans. *J. Turbomach.* **2022**, *144*, 091008. [CrossRef]
4. Hourmouziadis, J. Aerodynamic Design of Low Pressure Turbines. In *Blading Design for Axial Turbomachines*; AGARD Lecture Series; AGARD: Neuilly-sur-Seine, France, 1989.
5. Malzacher, F.J.; Gier, J.; Lippl, F. Aerodesign and Testing of an Aeromechanically Highly Loaded LP Turbine. *J. Turbomach.* **2003**, *128*, 643–649. [CrossRef]
6. Giovannini, M.; Rubechini, F.; Marconcini, M.; Arnone, A.; Bertini, F. Analysis of a LPT Rotor Blade for a Geared Engine: Part I—Aero-Mechanical Design and Validation. In Proceedings of the ASME Turbo Expo 2016: Turbomachinery Technical Conference and Exposition, Seoul, Republic of Korea, 13–17 June 2016. [CrossRef]
7. Hodson, H.P.; Dominy, R.G. Three-Dimensional Flow in a Low-Pressure Turbine Cascade at Its Design Condition. *J. Turbomach.* **1987**, *109*, 177–185. [CrossRef]
8. Vera, M.; Hodson, H.P.; Vazquez, R. The Effect of Mach Number on LP Turbine Wake–Blade Interaction. In *Unsteady Aerodynamics, Aeroacoustics and Aeroelasticity of Turbomachines*; Hall, K.C., Kielb, R.E., Thomas, J.P., Eds.; Springer: Dordrecht, The Netherlands, 2006; pp. 203–216.
9. Vázquez, R.; Antoranz, A.; Cadrecha, D.; Armananzas, L. The Influence of Reynolds Number, Mach Number and Incidence Effects on Loss Production in Low Pressure Turbine Airfoils. In Proceedings of the ASME Turbo Expo 2006, Barcelona, Spain, 6–11 May 2006; pp. 949–960. [CrossRef]
10. Perdichizzi, A. Mach Number Effects on Secondary Flow Development Downstream of a Turbine Cascade. *J. Turbomach.* **1990**, *112*, 643–651. [CrossRef]
11. Vázquez, R.; Torre, D. The Effect of Mach Number on the Loss Generation of LP Turbines. In Proceedings of the ASME Turbo Expo 2012, Copenhagen, Denmark, 11–15 June 2012; pp. 1131–1142. [CrossRef]
12. Hodson, H.P.; Dominy, R.G. The Off-Design Performance of a Low-Pressure Turbine Cascade. *J. Turbomach.* **1987**, *109*, 201–209. [CrossRef]
13. Duden, A.; Fottner, L. Influence of Taper, Reynolds Number and Mach Number on the Secondary Flow Field of a Highly Loaded Turbine Cascade. *Proc. IMechE Part A* **1997**, *211*, 309–320. [CrossRef]
14. Lopes, G.; Simonassi, L.; Torre, A.F.M.; Patinios, M.; Lavagnoli, S. An Experimental Test Case for Transonic Low-Pressure Turbines—Part 2: Cascade Aerodynamics at On- and Off-Design Reynolds and Mach Numbers. In Proceedings of the ASME Turbo Expo 2022, Rotterdam, The Netherlands, 13–17 June 2022. [CrossRef]
15. Lavagnoli, S.; Lopes, G.; Simonassi, L.; Torre, A.F.M. SPLEEN—High Speed Turbine Cascade—Test Case Database. *Zenodo* **2024**, Version v5, Published 9 September 2024. Available online: https://zenodo.org/records/13712768 (accessed on 29 January 2026).
16. Lopes, G.; Simonassi, L.; Gendebien, S.; Torre, A.F.M.; Patinios, M.; Zeller, N.; Pintat, L.; Lavagnoli, S. An Open Test Case for High-Speed Low-Pressure Turbines: The SPLEEN C1 Cascade. *Int. J. Turbomach. Propuls. Power* **2025**, *10*, 2. [CrossRef]
17. Pfeil, H.; Herbst, R.; Schröder, T. Investigation of the Laminar–Turbulent Transition of Boundary Layers Disturbed by Wakes. *J. Eng. Power* **1983**, *105*, 130–137. [CrossRef]
18. Lopes, G. Aerodynamics of a High-Speed Low-Pressure Turbine Cascade with Unsteady Wakes and Purge Flow. Ph.D. Thesis, Université de Liège, Liège, Belgium, 2024. Available online: https://zenodo.org/records/13712403 (accessed on 29 January 2026).
19. Lopes, G.; Simonassi, L.; Lavagnoli, S. Impact of Unsteady Wakes on the Secondary Flows of a High-Speed Low-Pressure Turbine Cascade. *Int. J. Turbomach. Propuls. Power* **2023**, *8*, 36. [CrossRef]
20. Simonassi, L.; Lopes, G.; Lavagnoli, S. Effects of Periodic Incoming Wakes on the Aerodynamics of a High-Speed Low-Pressure Turbine Cascade. *Int. J. Turbomach. Propuls. Power* **2023**, *8*, 35. [CrossRef]
21. Lopes, G.; Simonassi, L.; Lavagnoli, S. Time-Averaged Aerodynamics of a High-Speed Low-Pressure Turbine Cascade With Cavity Purge and Unsteady Wakes. *J. Turbomach.* **2023**, *146*, 021008. [CrossRef]
22. Youngren, H.; Drela, M. Viscous/Inviscid Method for Preliminary Design of Transonic Cascades. In Proceedings of the 27th Joint Propulsion Conference, Sacramento, CA, USA, 24–26 June 1991. [CrossRef]

23. Abu-Ghannam, B.J.; Shaw, R. Natural Transition of Boundary Layers—The Effects of Turbulence, Pressure Gradient, and Flow History. *J. Mech. Eng. Sci.* **1980**, *22*, 213–228. [CrossRef]
24. Drela, M. MISES Implementation of Modified Abu–Ghannam/Shaw Transition Criterion. In *MISES User's Guide*; MIT: Cambridge, MA, USA, 1995.
25. Langtry, R.B.; Menter, F.R. Correlation-Based Transition Modeling for Unstructured Parallelized Computational Fluid Dynamics Codes. *AIAA J.* **2009**, *47*, 2894–2906. [CrossRef]
26. Langtry, R.B. A Correlation-Based Transition Model Using Local Variables for Unstructured Parallelized CFD Codes. Ph.D. Thesis, University of Stuttgart, Stuttgart, Germany, 2006. Available online: http://elib.uni-stuttgart.de/opus/volltexte/2006/2801/ (accessed on 29 January 2026).
27. Coull, J.D.; Hodson, H.P. Predicting the Profile Loss of High-Lift Low Pressure Turbines. *J. Turbomach.* **2011**, *134*, 021002. [CrossRef]
28. Pastorino, G.; Simonassi, L.; Lopes, G.; Boufidi, E.; Fontaneto, F.; Lavagnoli, S. Measurements of Turbulence in Compressible Low-Density Flows at the Inlet of a Transonic Linear Cascade With and Without Unsteady Wakes. *J. Turbomach.* **2024**, *146*, 071002. [CrossRef]
29. Praisner, T.J.; Clark, J.P. Predicting Transition in Turbomachinery—Part I: A Review and New Model Development. *J. Turbomach.* **2004**, *129*, 1–13. [CrossRef]
30. Roach, P.E. The generation of nearly isotropic turbulence by means of grids. *Int. J. Heat Fluid Flow* **1987**, *8*, 82–92. [CrossRef]
31. Babajee, J.; Arts, T. Investigation of the Laminar Separation-Induced Transition with the γ–$\tilde{R}e_{\theta t}$ Transition Model on Low-Pressure Turbine Rotor Blades at Steady Conditions. In Proceedings of the ASME Turbo Expo 2012, Copenhagen, Denmark, 11–15 June 2012; pp. 1167–1178. [CrossRef]
32. Schlichting, H.; Gersten, K. *Boundary Layer Theory*; Springer: Berlin/Heidelberg, Germany, 2016.
33. Rosafio, N.; Lopes, G.; Salvadori, S.; Lavagnoli, S.; Misul, D.A. RANS Prediction of loss and Transition Onset in a High-Speed Low-Pressure Turbine Cascade. *Energies* **2023**, *16*, 7348. [CrossRef]
34. Mayle, R.E. The 1991 IGTI Scholar Lecture: The Role of Laminar–Turbulent Transition in Gas Turbine Engines. *J. Turbomach.* **1991**, *113*, 509–536. [CrossRef]
35. Hatman, A.; Wang, T. A Prediction Model for Separated-Flow Transition. *J. Turbomach.* **1999**, *121*, 594–602. [CrossRef]
36. Michálek, J.; Monaldi, M.; Arts, T. Aerodynamic Performance of a Very High Lift Low Pressure Turbine Airfoil (T106C) at Low Reynolds and High Mach Number with Effect of Free Stream Turbulence Intensity. *J. Turbomach.* **2012**, *134*, 061009. [CrossRef]
37. Houtermans, R.; Coton, T.; Arts, T. Aerodynamic Performance of a Very High Lift LP Turbine Blade with Emphasis on Separation Prediction. In Proceedings of the ASME Turbo Expo 2003, Atlanta, GA, USA, 16–19 June 2003; pp. 339–349. [CrossRef]
38. Ainley, D.G.; Mathieson, G.C.R. *A Method of Performance Estimation for Axial-Flow Turbines*; Aeronautical Research Council Reports and Memoranda No. 2974; Her Majesty's Stationery Office: London, UK, 1951.
39. Kacker, S.C.; Okapuu, U. A Mean Line Prediction Method for Axial Flow Turbine Efficiency. *J. Eng. Power* **1982**, *104*, 111–119. [CrossRef]
40. Zhu, J.; Sjolander, S.A. Improved Profile Loss and Deviation Correlations for Axial–Turbine Blade Rows. In Proceedings of the ASME Turbo Expo 2005, Reno, NV, USA, 6–9 June 2005; pp. 783–792. [CrossRef]
41. Dunham, J.; Came, P.M. Improvements to the Ainley–Mathieson Method of Turbine Performance Prediction. *J. Eng. Power* **1970**, *92*, 252–256. [CrossRef]
42. Benner, M.W.; Sjolander, S.A.; Moustapha, S.H. An Empirical Prediction Method for Secondary loss in Turbines—Part I: A New Loss Breakdown Scheme and Penetration Depth Correlation. *J. Turbomach.* **2006**, *128*, 273–280. [CrossRef]
43. Benner, M.W.; Sjolander, S.A.; Moustapha, S.H. An Empirical Prediction Method for Secondary loss in Turbines—Part II: A New Secondary Loss Correlation. *J. Turbomach.* **2006**, *128*, 281–291. [CrossRef]
44. Craig, H.R.M.; Cox, H.J.A. Performance Estimation of Axial Flow Turbines. *Proc. IMechE* **1970**, *185*, 407–424. [CrossRef]
45. Traupel, W. *Thermische Turbomaschinen: Band 1: Thermodynamisch–Strömungstechnische Berechnung*; Springer: Berlin/Heidelberg, Germany, 2019.
46. Senior, A.; Miller, R. A Data-Centric Approach to Loss Mechanisms. *J. Turbomach.* **2023**, *146*, 041007. [CrossRef]
47. Melzer, A.P.; Pullan, G. The Role of Vortex Shedding in the Trailing Edge Loss of Transonic Turbine Blades. *J. Turbomach.* **2019**, *141*, 041001. [CrossRef]
48. Rossiter, A.D.; Pullan, G.; Melzer, A.P. The Influence of Boundary Layer State and Trailing Edge Wedge Angle on the Aerodynamic Performance of Transonic Turbine Blades. *J. Turbomach.* **2022**, *145*, 041008. [CrossRef]
49. Pohlhausen, K. Zur näherungsweisen Integration der Differentialgleichung der laminaren Grenzschicht. *ZAMM* **1921**, *1*, 252–290. [CrossRef]
50. Timman, R. *A One Parameter Method for the Calculation of Laminar Boundary Layers*; National Aeronautical Research Institute: Amsterdam, The Netherlands, 1948.
51. Walz, A. Ein neuer Ansatz für das Geschwindigkeitsprofil der laminaren Reibungsschicht. *Lilienthal-Bericht* **1941**, *141*, 1–8.

52. Thwaites, B. Approximate Calculation of the Laminar Boundary Layer. *Aeronaut. Q.* **1949**, *1*, 245–280. [CrossRef]
53. Curle, N.; Skan, S.W. Approximate Methods for Predicting Separation Properties of Laminar Boundary Layers. *Aeronaut. Q.* **1957**, *8*, 257–268. [CrossRef]
54. Stratford, B.S.; Gadd, G.E. *Flow in the Laminar Boundary Layer Near Separation*; Report No. 3002; Aeronautical Research Council, Ministry of Supply: London, UK, 1954.
55. Coull, J.D. Endwall Loss in Turbine Cascades. *J. Turbomach.* **2017**, *139*, 081004. [CrossRef]
56. Denton, J.D. The 1993 IGTI Scholar Lecture: Loss Mechanisms in Turbomachines. *J. Turbomach.* **1993**, *115*, 621–656. [CrossRef]
57. Torre, A.F.M.; Patinios, M.; Lopes, G.; Simonassi, L.; Lavagnoli, S. Vane–Probe Interactions in Transonic Flows. *J. Turbomach.* **2023**, *145*, 061010. [CrossRef]
58. Lopes, G.; Simonassi, L.; Torre, A.F.M.; Lavagnoli, S. Instrumentation Interference in a Transonic Linear Cascade. *J. Phys. Conf. Ser.* **2023**, *2511*, 012018. [CrossRef]
59. Coull, J.D.; Clark, C.J. The Effect of Inlet Conditions on Turbine Endwall Loss. *J. Turbomach.* **2022**, *144*, 101011. [CrossRef]

Disclaimer/Publisher's Note: The statements, opinions and data contained in all publications are solely those of the individual author(s) and contributor(s) and not of MDPI and/or the editor(s). MDPI and/or the editor(s) disclaim responsibility for any injury to people or property resulting from any ideas, methods, instructions or products referred to in the content.